*inorganics*

MDPI

*Review*

# Magnetic Modulation of Catalytic $CO_2$ Reduction Reaction: Mechanisms, Strategies, and Perspectives

**Dongqiu Zhao [1,†], Shannan Xu [1,†], Mei Bie [2], Chunyi Ma [1], Huahua Fan [3] and Lin Ju [1,*]**

[1] Anyang Key Laboratory of Optoelectronic Information Materials, Anyang Key Laboratory of Novel Functional Materials and Device Design, School of Physics and Telecommunication Engineering, Anyang Normal University, Anyang 455000, China; dqzhao@aynu.edu.cn (D.Z.); 211103007@stu.aynu.edu.cn (S.X.); 241104050@stu.aynu.edu.cn (C.M.)
[2] Shandong Institute for Food and Drug Control, Jinan 250101, China; bm19861208@163.com
[3] College of Chemistry and Chemical Engineering, Anyang Normal University, Anyang 455000, China; fanhuahua1996@aynu.edu.cn
* Correspondence: julin@aynu.edu.cn
† These authors contributed equally to this work.

## Abstract

Catalytic $CO_2$ reduction reaction ($CO_2$RR) offers a promising approach for converting $CO_2$ into value-added chemicals and fuels. However, its practical development remains limited by unfavorable reaction energetics, competition from the hydrogen evolution reaction (HER), and complex product selectivity. Conventional catalyst regulation strategies predominantly rely on static structural design, whereas magnetic regulation introduces an additional degree of freedom through intrinsic spin-state engineering or external magnetic fields. This review systematically summarizes the recent research progress in magnetic regulation of $CO_2$RR with emphasis on the links among spin states, spin-resolved electronic structures, intermediate adsorption, reaction thermodynamics, product selectivity, competing reactions, and charge-carrier dynamics. Importantly, catalytic changes induced by an external magnetic field are not automatically equivalent to spin-mediated effects because magnetohydrodynamic transport, Lorentz-force-driven mass transfer, thermal perturbations, and interfacial transport can also contribute. The review therefore discusses both intrinsic magnetic regulation and field-induced effects while highlighting the evidence required to distinguish spin-associated mechanisms from non-spin contributions, including direct magnetic or spin characterization, spectroscopic evidence, and electrochemical controls that assess transport and thermal effects. Strategies including doping, vacancies, heterojunctions, axial coordination, defect engineering, and applied magnetic fields are summarized, followed by perspectives on physics-informed machine learning, artificial intelligence, and operando sensing for catalyst screening and dynamic regulation.

**Keywords:** $CO_2$RR; magnetic regulation; spin polarization

Check for updates

Academic Editor: Maurizio Peruzzini

Received: 3 September 2026
Revised: 1 October 2026
Accepted: 3 October 2026
Published: 5 October 2026

**Copyright:** © 2026 by the authors. Licensee MDPI, Basel, Switzerland. This article is an open access article distributed under the terms and conditions of the Creative Commons Attribution (CC BY) license.

## 1. Introduction

With the accelerating pace of worldwide industrial growth, the extensive use of fossil fuels has led to a sustained rise in atmospheric $CO_2$ concentrations, giving rise to severe global warming and climate-related issues. Among the various $CO_2$ conversion technologies, catalytic $CO_2$ reduction reaction ($CO_2$RR) has attracted considerable attention owing to its capability to transform $CO_2$ into high-value-added fuels and chemicals, such

as $CH_4$ [1], CO [2], $CH_3OH$ [3,4], $C_2H_4$ [5], $C_2H_5OH$ [6]. However, the $CO_2RR$ still faces numerous challenges, primarily including unfavorable reaction thermodynamics [7–9], severe competition from hydrogen evolution [10–12], and poor product selectivity [13]. To address these challenges, researchers have conducted extensive explorations across various aspects of catalyst design [14–18].

In terms of catalyst composition, catalytic performance has been optimized by tuning the elemental species of active sites [19,20] and their coordination environments [21–24]. For example, the precise design of metal centers and coordinating atoms in single-atom catalysts can significantly alter the selectivity of $CO_2RR$ [25–28], while dual-atom catalysts further modulate the adsorption configurations and reaction pathways of intermediates through the synergistic effects of bimetallic sites [29–32]. With respect to catalyst morphology, facet engineering enables the exposure of more highly active sites [33–35]. In terms of interface engineering, the construction of heterojunctions or the introduction of surface modification layers can regulate the local environment and stabilize intermediates, thereby enhancing $CO_2RR$ selectivity [36–38]. Collectively, these studies have demonstrated the close links between the electronic structures of catalysts and their catalytic performance, substantially advancing the development of $CO_2RR$ catalysts. However, most of these regulation strategies rely on the static intrinsic structures of catalysts, which are difficult to be flexibly modulated during the reaction process. Therefore, exploring an approach that enables dynamic modulation of catalyst electronic states under external stimuli to optimize catalytic performance has become an important research direction [39].

In recent years, magnetic regulation has emerged as a novel approach to improve catalytic performance and gradually attracted increasing attention [40–42]. Intrinsic magnetic regulation tailors the spin states [43–45], spin polarization [46,47], magnetic moments, and spin-resolved orbital interactions of active sites, thereby governing intermediate adsorption and reaction pathways. In contrast to these intrinsic approaches, external magnetic fields offer a complementary yet distinct strategy that can perturb magnetic domains and spin populations. However, they may also modify mass transport and interfacial processes through non-spin mechanisms such as magnetohydrodynamic effects. Consequently, an improvement in $CO_2RR$ performance under a magnetic field should not by itself be regarded as proof of a spin-mediated mechanism. This review considers both electrocatalytic and photocatalytic $CO_2RR$ (as shown in Figure 1), where spin-polarized carrier dynamics are central. This regulatory approach exhibits unique advantages in enhancing catalytic activity [48], tailoring product selectivity [49] and suppressing competing reactions [50]. The discussion first summarizes the principal magnetic and spin-related mechanisms, then reviews practical strategies for tuning magnetic properties, and finally evaluates how these effects influence adsorption, selectivity, C-C coupling, the competing hydrogen evolution reaction, and charge-carrier dynamics. Particular attention is given to distinguishing spin-associated effects from magnetohydrodynamic, Lorentz-force-driven, thermal, and interfacial transport contributions under external magnetic fields. This evidence-based framing provides a clearer basis for evaluating reported magnetic effects and for identifying future directions in magnetic catalyst design.

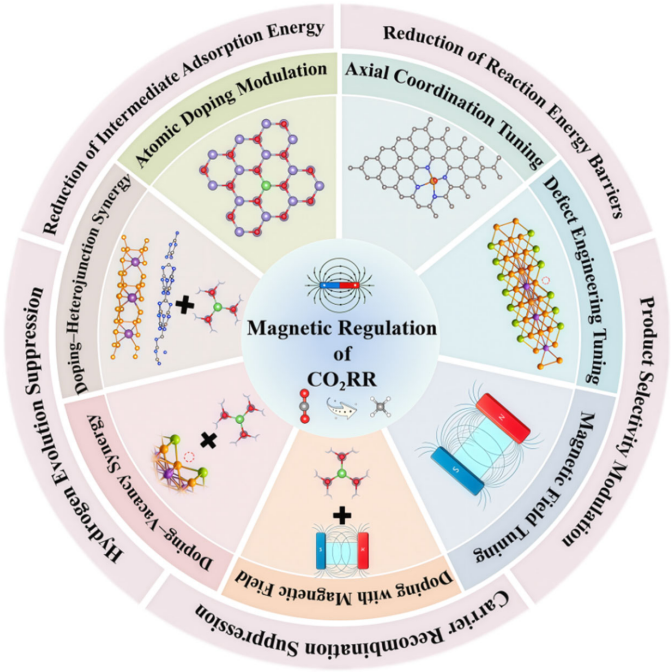



**Figure 1.** This review systematically presents the regulatory strategies and underlying mechanisms of magnetic modulation in $CO_2RR$. Reproduced with permissions [44,51]. Copyright 2025, American Chemical Society.

## 2. Magnetic Regulation Mechanisms of $CO_2RR$

### *2.1. Modulating Intermediate Adsorption Energy via Spin States*

In catalytic reactions, reactant molecules must first adsorb onto the catalyst surface before the reaction can proceed, and the adsorption strength [52] directly influences both the reaction feasibility [53] and the selectivity of reaction pathways [54]. For transition-metal active sites, adsorption is often discussed in terms of hybridization between metal *d* states and adsorbate orbitals. Spin-state changes can modify orbital occupancy, exchange splitting, and the relative energies of spin-up and spin-down *d* states, thereby altering metal-adsorbate bonding. In a ligand field, high-spin, intermediate-spin, and low-spin configurations correspond to different occupations of split *d* orbitals, and these changes can modify both the spatial availability of orbitals and their energy alignment with adsorbates. The conventional *d*-band center represents an average over the *d* states, whereas a spin-polarized catalyst can require separate consideration of spin-up and spin-down *d*-band centers because the two channels may interact differently with an adsorbate. Therefore, adsorption trends should be interpreted through spin-resolved orbital occupation and hybridization rather than through a universal assumption that a given spin state always strengthens or weakens adsorption. The *d*-band picture is also not universally sufficient. For active sites with substantial *p*-orbital contributions, including *p*-block elements and mixed *p*-*d* systems, *p*-derived states and *p*-*d* coupling can become relevant descriptors [55]. The relevance of these descriptors can in turn be modulated by external or structural factors. Structural perturbations such as strain, curvature, and coordination changes can further modify orbital splitting, bandwidth, and local spin polarization. The curvature-engineered SiFe dual-atom system [56] provides a compelling illustration of this point. In this system, purely geometric modulation of the carbon support shifts the Si *p*-band center downward by 1.43 eV while the Fe *d*-band center shifts downward by only 0.36 eV. This downward shift strengthens the interaction between the Si site and oxygenated intermediates, making the Si site the dominant adsorption site for *OH and *$H_2O$, which are the key species that define the PDS. Notably, the magnetic moment of this system remains essentially constant

at approximately 2 μB across the entire curvature range, indicating that the enhanced activity originates primarily from geometric and *p*-band effects rather than spin-state changes. This example is included not as a case of magnetic regulation, but to underscore that geometric and electronic effects beyond spin and *d*-band, such as *p*-band modulation, can also profoundly influence catalytic performance and should therefore be considered alongside magnetic descriptors when evaluating complex catalytic systems. Therefore, when relating magnetic descriptors to adsorption behavior, all these factors, including spin state, spin-resolved *d*-band centers, *p*-band descriptors, *p*-*d* coupling, and structural perturbations, should be considered together rather than relying on any single descriptor in isolation.

For catalytic $CO_2$RR, different reaction pathways proceed through distinct intermediates [57]. Spin-state regulation can modify the adsorption energetics of pathway-specific intermediates and thereby shift their relative thermodynamic favorability. Taking the ferromagnetic catalyst Ni@NC as an example, the modulation of the Ni electronic structure by an external magnetic field was associated with changes in orbital occupation and the *d*-band center. As shown in Figure 2a, the $t_{2g}$ and $d_{z^2}$ orbitals of Ni are fully occupied, while the $d_{x^2-y^2}$ orbital remains available for interaction with $CO_2$. Without a magnetic field, the *d*-band center of Ni is located at −1.34 eV, resulting in weak adsorption of *COOH. Under an applied magnetic field, spin polarization modifies the *d*-band center upward to −0.98 eV, significantly enhancing the adsorption strength, accompanied by stronger *COOH adsorption [58]. In the $Cu_2O$ system, the magnetic field similarly alters the adsorption characteristics of intermediates. As shown in Figure 2b, application of a 3 T magnetic field changes the calculated free energy requirements associated with *OCHO and *COOH formation from 0.078 to 0.325 eV and from 0.568 to 0.817 eV, respectively [59]. These examples show that magnetic regulation can alter intermediate energetics, although the direction and magnitude of the response remain system dependent.

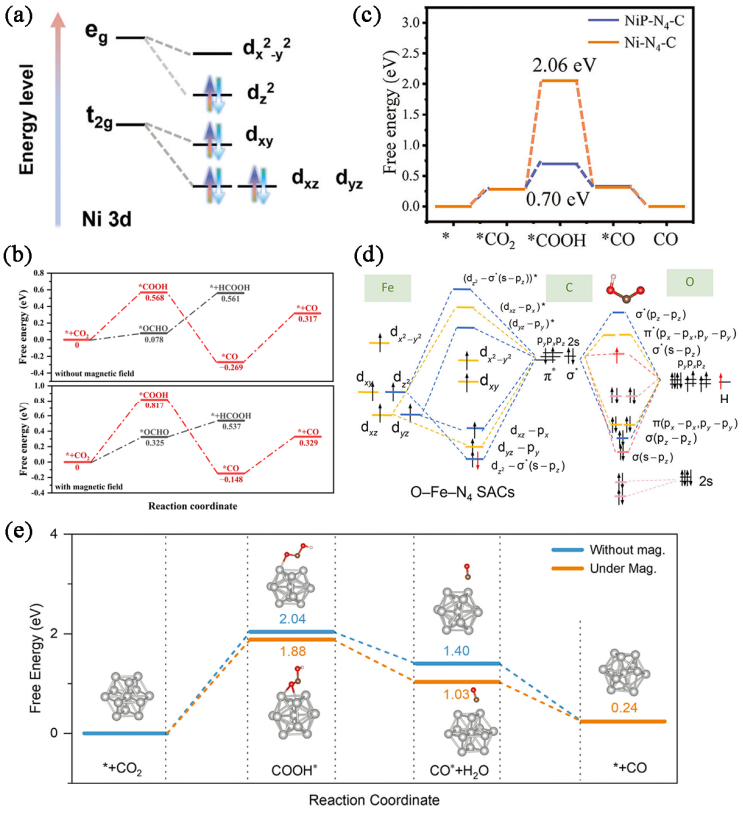



**Figure 2.** (**a**) Schematic diagram of the *d*-orbital electronic configuration of Ni atoms. (**a**,**e**) Reproduced with permission [58]. Copyright 2024, Wiley-VCH GmbH; (**b**) Free energy diagrams of the CO and

HCOOH pathways. (**b**) Reproduced with permission [59]. Copyright 2023, MDPI; (**c**) Free energy diagrams of CO formation on Ni-$N_4$-C and NiP-$N_4$-C. (**c**) Reproduced with permission [27]. Copyright 2024, Wiley-VCH GmbH; (**d**) Schematic illustration of molecular orbital interactions between Fe and *COOH in O-Fe-$N_4$. (**d**) Reproduced with permission [60]. Copyright 2026, Wiley-VCH GmbH; (**e**) Free energy diagrams of Ni@NC for CO formation with and without an external magnetic field. * stands for the adsorption site at the surface of catalyst.

### *2.2. Modulating Reaction Thermodynamics via Spin Polarization*

In the $CO_2$ reduction to CO, the generation of the *COOH intermediate from $CO_2$ is believed to be the potential-determining step (PDS) [61]. This step involves the transfer of one electron and one proton to $CO_2$ [62], and consequently the free energy change ($\Delta G$) of this step directly dictates the overall thermodynamic free energy requirement and the required overpotential. Based on the aforementioned mechanism of spin-state modulation of intermediate adsorption energy, this section focuses on *COOH to analyze the way in which spin polarization reduces the uphill free energy requirement of the PDS by tuning its adsorption strength. The spin polarization effect corresponding to the high-spin state can significantly reduce this thermodynamic free energy requirement. Spin-state-dependent changes in *d*-orbital occupancy, *d-p* hybridization, and charge transfer can modify the stabilization of *COOH and thereby change the free energy requirement of the proton-electron transfer step. In specific systems, orbital-resolved calculations further indicate enhanced interaction between metal *d* states and adsorbate orbitals. The spin-state transition induced by axial coordination can effectively reduce the thermodynamic free energy requirement. Specifically, Ni in Ni-$N_4$-C is in a low-spin state with zero unpaired electrons. After axial P coordination, NiP-$N_4$-C transitions to a high-spin state with the population of unpaired electrons increasing to two. The corresponding free energy diagrams (Figure 2c) reveal that the free energy of *COOH on Ni-$N_4$-C is as high as 2.06 eV, whereas that on NiP-$N_4$-C is significantly reduced to 0.70 eV [27]. Sun et al. [60] also achieved a high-spin state of Fe through axial O coordination. The bonding orbital schematic in Figure 2d and the corresponding free energy diagrams show that the high-spin configuration enhances the interaction between Fe and *COOH, substantially reducing the free energy requirement for *COOH formation. The application of an external magnetic field also serves to decrease the free energy for *COOH formation via spin polarization. As depicted in the free energy diagram (Figure 2e), the $\Delta G$ for *COOH formation is reduced from 2.04 eV to 1.88 eV [58]. These results support a thermodynamic role of spin-state regulation, while kinetic acceleration should only be claimed when an activation barrier has been directly evaluated.

### *2.3. Tuning of Product Selectivity by Spin States*

Product selectivity in $CO_2$RR could be influenced by spin state together with the coordination environment, electrode potential, pH, electrolyte composition, and intermediate coverage [63]. The effects of these factors on selectivity are largely realized by altering the adsorption behavior of key intermediates, among which *CO is the crucial intermediate determining product distribution [64]. Because it can desorb as CO, be further hydrogenated to more deeply reduced $C_1$ products, or participate in C-C coupling to form $C_{2+}$ products [65,66]. Research indicates that the spin state is closely linked to both *CO adsorption behavior and product selectivity, with the underlying regulatory mechanism differing among catalytic systems. In the Ni-Mn dual-atom catalyst, the spin-state transition of Mn induced by axial coordination significantly affects the product selectivity. As shown in Figure 3a, Mn in the Mn single-atom catalyst (SAC) is in a low-spin state with one unpaired electron. After axial Ni coordination, Mn in the Ni-Mn dual-atom catalyst (DAC) transitions to a high-spin state with three unpaired electrons and shifts the *d*-band center toward the

Fermi level. This electronic structural change enhances the adsorption capacity of Mn sites toward *CO, allowing a portion of the *CO to undergo further hydrogenation to produce $CH_4$. Product selectivity analysis reveals that at −0.7 V, the Ni-Mn DAC achieves a CO Faradaic efficiency (FE) of 86.6% and can further steer the selectivity toward $CH_4$, whereas the Mn-Ni DAC produces only CO [67]. This case demonstrates that spin-state transitions can enhance *CO adsorption to a certain extent, enabling a portion of *CO to undergo further hydrogenation toward $CH_4$. Beyond intrinsic spin-state engineering, external fields can also modulate product selectivity through spin-related mechanisms. The projected density of states (PDOS) plots in Figure 3b reveal that the spin-up and spin-down electron distributions of Cu in the Cu metal–organic framework (MOF) are largely symmetric, indicating weak spin polarization. Upon incorporation of Zn/Mg, the Cu-ZnMg MOF exhibits a pronounced asymmetric spin distribution with significantly enhanced spin polarization. The applied AMF, via spin-lattice relaxation, interacts with the spin magnetic moments of the isolated Cu sites, leading to a local rise in electronic energy. Such a rise not only boosts proton generation but also expedites charge-migration kinetics, both of which contribute to an enhanced $CO_2$-to-CO conversion performance. ATR-FTIR results show that the signal of the *COOH intermediate on Cu-ZnMg MOF is significantly stronger than that on Cu MOF, while the *CO signal is considerably weaker, indicating that spin polarization is closely associated with enhanced *COOH formation and facilitated *CO desorption in this system. The corresponding product selectivity is presented in Figure 3c. At −0.6 V, the Cu-ZnMg MOF achieves a CO FE of approximately 92%, accompanied by only small amounts of $H_2$ and $C_2H_4$. In contrast, the Cu MOF generates substantial $H_2$ and $C_2H_4$ with only a trace amount of CO [68].

Recent $CO_2$RR studies have shown that regulating the adsorption configuration of *CO also can enhance $C_2H_5OH$ selectivity. For instance, Xiong et al. [69] encapsulated Cu nanowires with a PANI shell, which shifts *CO adsorption from atop to bridge sites and minimizes the C-C coupling barrier when the ratio of atop- to bridge-bonded *CO reaches approximately 1:3, thereby accelerating subsequent hydrogenation toward $C_2H_5OH$. Meanwhile, Zn doping has been shown to steer Cu-based catalysts toward $C_2H_5OH$ by modifying the reaction pathway. Zang et al. [70] demonstrated that Zn incorporation modulates the electronic structure of Cu while promoting high-index step sites, enabling asymmetric *CO adsorption and stabilizing the *CHCOOH intermediate to favor $C_2H_5OH$ formation. It should be noted that the PANI-encapsulated Cu nanowires and Zn-doped Cu systems discussed above are included as nonmagnetic benchmarks, rather than as examples of magnetic regulation. These nonmagnetic studies reveal the key controlling factors for $C_2$ product formation, namely *CO coverage, C-C coupling efficiency, and protonation steps. Systematic exploration of $C_2$ pathways in magnetic systems has not yet been reported, and these key factors hold promise for further optimizing $C_2$ product selectivity through spin polarization.

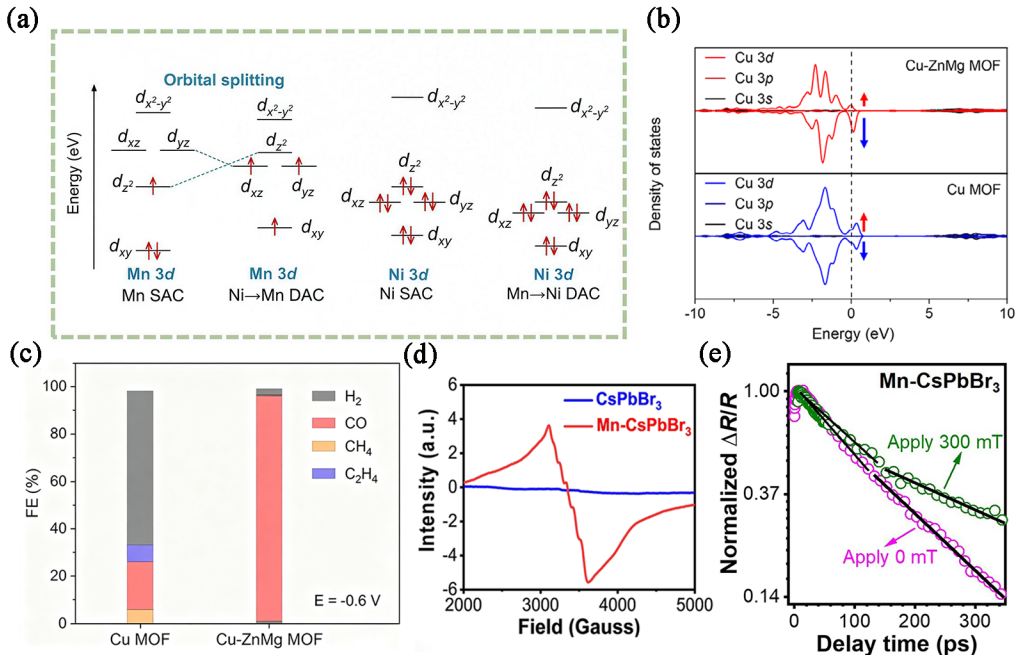



**Figure 3.** (**a**) Comparison of Mn 3*d* orbital splitting in Ni-Mn DAC and Mn SAC. (**a**) Reproduced with permission [67]. Copyright 2025, Wiley-VCH GmbH; (**b**) PDOS comparison of Cu sites in Cu MOF and Cu-ZnMg MOF; (**c**) Product FE of Cu MOF and Cu-ZnMg MOF at −0.6 V. (**b**,**c**) Reproduced with permission [68]. Copyright 2025, Wiley-VCH GmbH; (**d**) Electron paramagnetic resonance spectra of $CsPbBr_3$ and Mn-$CsPbBr_3$; (**e**) Transient reflectivity change curves of Mn-$CsPbBr_3$ with and without a magnetic field. (**d**,**e**) Reproduced with permission [71]. Copyright 2022, American Chemical Society.

### *2.4. Suppressing HER via Spin Effects*

In addition to carbon-containing intermediates, *H adsorption is a central factor governing competition from the hydrogen evolution reaction (HER). In $CO_2$RR, HER is the most significant competing side reaction, and its first step involves $H^+$ in the solution acquiring an electron, thereby forming an adsorbed H atom on the catalyst surface [72,73]. Spin polarization can change the electronic configuration of a metal active site and thereby modify metal-H orbital hybridization, the occupation of bonding and antibonding states, and the adsorption free energy of *H. HER suppression should therefore be interpreted in terms of changes in $\Delta G$ (*H) and competitive adsorption rather than as a universal direct repulsion between a H electron and unpaired metal *d* electrons. For example, under an external magnetic field applied to the Ni-$N_5$-C catalyst, the slope of the $1/\chi$-T curve in the low-temperature region changes in the presence of the magnetic field, indicating enhanced spin polarization. The corresponding free energy diagrams show that the adsorption free energy of *H is 0.76 eV in the absence of a magnetic field, and increases to 0.85 eV upon application of the magnetic field, which makes H adsorption less thermodynamically favorable relative to the field-free condition [40]. In the $Cu_2O$ system, an external magnetic field can also suppress the HER. At −1.0 and −1.1 V versus RHE, the FE of $H_2$ upon application of a 3 T magnetic field is significantly lower than that in the absence of the magnetic field, indicating that the HER is suppressed [59]. These observations are consistent with suppression of the competing HER, although the relative contributions of spin-state changes, interfacial transport, and other field-induced effects should be considered for each system.

### *2.5. Suppressing Photogenerated Carrier Recombination via Spin Polarization*

In photocatalytic $CO_2$RR, the separation and recombination dynamics of photogenerated electrons and holes strongly affect the fraction of carriers that reach surface reaction sites, col-

lectively determining the photocatalytic efficiency [74–76]. Spin polarization can modify these dynamics because spin-selection rules may suppress or slow recombination channels that are spin-forbidden. When magnetic metal atoms are introduced into a semiconductor, the unpaired *d* electrons provided by these atoms undergo spin-exchange interactions with the free electrons in the semiconductor. This interaction splits the originally energy-degenerate spin-up and spin-down bands, resulting in asymmetric occupation of the valence band maximum (VBM) and conduction band minimum (CBM) by specific spin states. Under such a spin-polarized band structure, photoexcitation tends to generate electrons and holes with the same spin direction. Spin polarization can modify the availability and probability of spin-allowed recombination channels. Consequently, selected recombination pathways may be suppressed or slowed, which can prolong carrier lifetimes under appropriate electronic-structure conditions. This suppression is not absolute. Spin–orbit coupling, defects, phonon-assisted processes, and spin relaxation can relax the selection rules and open additional recombination pathways. Consequently, spin-polarized band structures should be interpreted as one factor controlling carrier lifetimes rather than as a complete prohibition of same-spin recombination. Spin polarization induced by doping has been demonstrated to suppress carrier recombination in several photocatalytic systems. In Co-doped CdS, density of states (DOS) calculations reveal that the spin DOS near the Fermi level exhibits pronounced asymmetry after Co doping, giving rise to spin polarization. Upon application of a 150 mT magnetic field, the photoluminescence (PL) intensity of 3Co-CdS decreases significantly, indicating a reduction in radiative recombination. Meanwhile, time-resolved photoluminescence (TR-PL) decay curves show a pronounced prolongation of carrier lifetime, suggesting a decreased recombination rate. Collectively, these observations support a spin-related suppression of photogenerated charge carrier recombination in this system [77]. Additionally, spin-polarization-suppressed carrier recombination is also observed in Mn-doped $CsPbBr_3$ nanoplatelets. The electron paramagnetic resonance (EPR) spectra in Figure 3d reveals that Mn-$CsPbBr_3$ exhibits a distinct EPR signal, whereas pristine $CsPbBr_3$ shows no signal, indicating that $Mn^{2+}$ doping introduces unpaired electrons and generates spin polarization. The transient reflectance (TR-R) curves show that the carrier decay in Mn-$CsPbBr_3$ is significantly slower than that in pristine $CsPbBr_3$, suggesting that spin polarization prolongs the carrier lifetime. Upon further application of a 300 mT magnetic field (Figure 3e), the decay in Mn-$CsPbBr_3$ becomes even slower, indicating that the external magnetic field enhances spin polarization and further suppresses carrier recombination [71]. Taken together, the catalytic, magnetic, and carrier-dynamic measurements are consistent with a spin-associated contribution in this photocatalytic system, although field-induced non-spin effects should still be considered when assigning causality.

## 3. Strategies for Modulating the Magnetic Properties of Catalysts

### *3.1. Doping-Based Magnetic Modulation*

Doping is one of the important strategies for modulating catalyst performance and enhancing the activity and selectivity of $CO_2RR$ [55,78–81]. By introducing magnetic metal atoms into the catalyst, the spin states of the *d*-orbital electrons at the metal active centers can be altered, thereby affecting the $CO_2RR$ performance [67]. Furthermore, the combination of doping with external magnetic fields, vacancies, heterojunctions, and other strategies can generate synergistic effects, thereby further enriching the approaches for magnetic modulation of $CO_2RR$.

#### 3.1.1. Magnetic Modulation via Heteroatom Doping

Atomic doping enhances $CO_2RR$ performance by manipulating the electronic structure, introducing additional active sites, and improving the adsorption performance of key intermediates. Moreover, when magnetic atoms or ions are introduced, doping can also

manipulate the magnetic properties of catalysts, providing an additional degree of freedom for catalytic regulation. Single-atom [82,83], dual-atom [56,84,85], and metal-ion doping are fundamental strategies for modulating the properties of catalysts. Especially when magnetic atoms (e.g., Fe, Co, Ni, Cu) or ions (e.g., $La^{3+}$, $Ni^{2+}$) are introduced into nonmagnetic or weakly magnetic substrates to create local magnetic moments at the atomic scale. On the basis of density functional theory (DFT), Koua et al. [86] reported that doping La atoms into the nonmagnetic $Ti_3C_2O_2$ MXene substrate can convert the originally nonmagnetic $Ti_3C_2O_2$ into a magnetic material, exhibiting two magnetic configurations, namely ferromagnetic (FM) with parallel alignment of adjacent magnetic moments and antiferromagnetic (AFM) with antiparallel alignment. The AFM configuration exhibits a $CO_2$ adsorption energy of −1.87 eV, and the reported free energy change associated with *OCHO formation is −1.94 eV, which is substantially lower than that of undoped $Ti_3C_2O_2$ (2.62 eV for *OCHO formation). It can be seen from the results that after La doping, the adsorption energy of $CO_2$ is much below that of $H^+$, and the $H^+$ adsorption energy of the AFM configuration is slightly higher than that of the FM configuration. The results suggest that the magnetic configuration introduced by La doping may contribute to lowering the free energy requirement of the PDS and to suppressing the competing HER. It should be noted that La doping also changes the local structure, surface oxygen configuration, charge distribution, and electronic structure of $Ti_3C_2O_2$, all of which can influence $CO_2$ adsorption and activation. The observed enhancement should therefore be considered together with these structural and electronic effects rather than attributed solely to the introduced magnetism. Liu et al. [44] substituted the Zn sites in tetrahedrally coordinated ZnO with 3*d* transition metal atoms (Mn, Fe, Co, Ni, and Cu) to construct tetrahedrally coordinated single-atom catalysts (TCSACs). A volcano-shaped correlation was found between the magnetic moments of these metal sites and the $CO_2$RR performance. As shown in Figure 4a, the magnetic moments of Mn, Fe, Co, and Ni are 4.58, 3.71, 2.57, and 0.99 μB, respectively, exhibiting an inverted volcano-shaped relationship with the limiting potential, with Fe located at the volcano peak. $Fe^{3+}$ is in an intermediate-spin state with a moderate magnetic moment, which leads to a reduction in the Gibbs free energy change for the conversion of the *COOH intermediate to *CO (the PDS) to 0.57 eV. Figure 4b shows that the Fe-doped tetrahedrally coordinated single-atom catalyst achieves a CO FE of 91.6% at −0.9 V. This result indicates that the adsorption behavior of reaction intermediates can be tuned by selecting dopant atoms with different magnetic moments, although the introduction of transition metal atoms also modifies the local coordination environment, charge distribution, and electronic structure of ZnO. Beyond single-metal doping, bimetallic element doping offers an additional strategy for introducing magnetic moments and tuning catalytic performance via spin-state engineering. Hu et al. [87] probed the effect of bimetallic element doping with $Fe_2$ and $Cu_2$ sites in g-$C_3N_4$ on photocatalytic $CO_2$-to-$C_2$ conversion. Calculations show that $Fe_2$ and $Cu_2$ sites exhibit pronounced spin polarization characteristics, with *d*-orbital hybridization interactions with $CO_2$ molecular orbitals that are superior to those of single-atom sites. The spin-up and spin-down DOS at the $Fe_2$ sites exhibit pronounced asymmetry, with stronger spin polarization than that at the $Cu_2$ sites, and the spin polarization mainly originates from the *d*-orbital contributions of Fe. For the C-C coupling step, the calculated $\Delta G$ are −1.5 eV on $Fe_2$ and −1.66 eV on $Cu_2$. Both negative values indicate that C-C coupling is thermodynamically favorable on both sites, with the high-spin state of $Fe_2$ possibly contributing to the selectivity toward $C_2$ products. Liao et al. [88] doped $Ni^{2+}$/$Ni^{3+}$ ions into the double perovskite $Sr_2Fe_{1.5}Mo_{0.5}O_6$-δ substrate to partially substitute Fe, and found that Ni doping induces a transition of Fe ions from high-spin $Fe^{3+}$ to high-spin $Fe^{4+}$. The magnetic hysteresis loops (M-H) in Figure 4c reveal that the slope of SFNM is greater than $SF_{1.5}M$, indicating an increase in unpaired electron count after Ni doping. The zero-field-cooled (ZFC) curves in Figure 4d further show that the magnetic susceptibility of SFNM is higher compared to that of $SF_{1.5}M$ over the entire temperature

range, supporting the interpretation that Ni doping enhances spin polarization. For high-spin $Fe^{4+}$, the *d* electrons fully occupy three low-energy orbitals, occupy only one electron in the high-energy orbitals, and leave another high-energy orbital vacant. This vacant orbital can accept the lone-pair electrons of the O atom in $CO_2$, thereby enhancing $CO_2$ adsorption. As shown in Figure 4e, the $CO_2$ adsorption energies at different sites on SFNM are significantly lower than those on $SF_{1.5}M$, with the Fe-O-Ni site reaching as low as −1.14 eV, far lower than the −0.32 eV of $SF_{1.5}M$. Meanwhile, the CO adsorption energy on SFNM is also significantly weakened. Weakened *CO adsorption facilitates the rapid desorption of CO from the catalyst surface, preventing the active sites from being occupied and deactivated by *CO, which may help maintain a high reaction rate and CO selectivity. Covalent organic frameworks (COFs) provide an additional platform in which the spin environment of molecularly defined active sites can be tuned without substantially changing the overall catalyst architecture [89]. A recent grid-like COF containing Co centers and semiquinone radicals was reported to form coupled dual-spin centers, where the organic radical spin density and a low-spin Co configuration jointly promoted $CO_2$ activation, *COOH formation, and *CO desorption. This type of system is particularly useful for magnetic $CO_2$RR because spectroscopic and theoretical spin descriptors are linked directly to elementary reaction steps rather than inferred only from changes in catalytic performance.

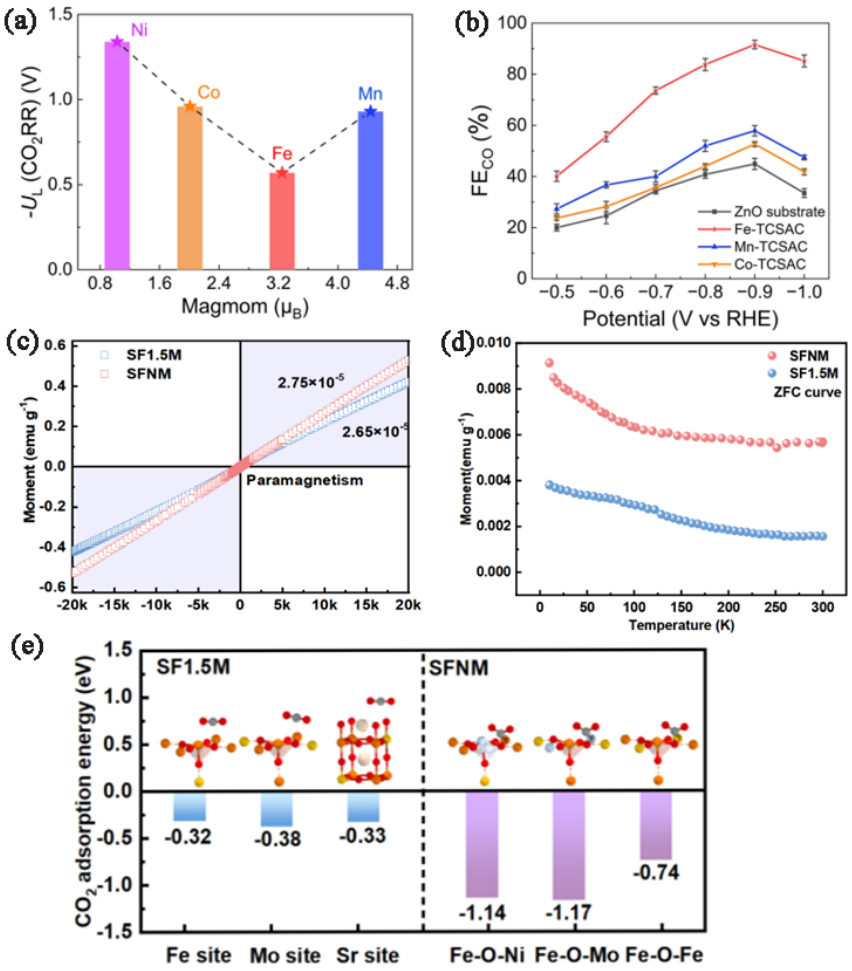



**Figure 4.** (**a**) Inverted volcano relationship between magnetic moment and limiting potential for different TM-TCSACs; (**b**) CO Faradaic efficiency of different TCSACs at various potentials. (**a**,**b**) Reproduced with permission [44]. Copyright 2025, American Chemical Society; (**c**) Magnetic hysteresis loops (M-H) of SFNM and $SF_{1.5}M$; (**d**) Enlarged ZFC curves of SFNM and $SF_{1.5}M$ [88]; (**e**) Comparison of $CO_2$ adsorption energies at different sites on SFNM and $SF_{1.5}M$. (**c**–**e**) Reproduced with permission [88]. Copyright 2025, American Chemical Society.

3.1.2. Magnetic Modulation via Synergy Between Doping and External Magnetic Field

On the basis of intrinsic magnetic moments introduced by atomic doping, the application of an external magnetic field can align these magnetic moments along the field orientation, thereby further enhancing spin polarization. This synergistic effect can more substantially inhibit photogenerated charge carrier recombination and prolong the carrier lifetime. Xiong et al. [77] investigated the synergistic effect between doping and an external magnetic field in the Co-doped CdS system. It is found that without a magnetic field, the CO yield of pristine CdS is only 212.6 μmol $g^{-1}$ $h^{-1}$, while the $H_2$ yield is as high as 1075.1 μmol $g^{-1}$ $h^{-1}$. As the Co doping level increases, the CO yield gradually increases, reaching 1366.8 μmol $g^{-1}$ $h^{-1}$ for 3Co-CdS, while the $H_2$ yield decreases to 389.9 μmol $g^{-1}$ $h^{-1}$. This indicates that Co doping itself can suppress the HER and promote $CO_2$RR. Upon application of a 150 mT external magnetic field, the CO yield of each Co-doped sample further increases. The CO yield of 3Co-CdS reaches 2322.8 μmol $g^{-1}$ $h^{-1}$, which is 1.7 times the value obtained without a magnetic field, while the $H_2$ yield further decreases. With increasing magnetic-field strength from 0 to 150 mT, the CO yield of 3Co-CdS continuously increases and the $H_2$ yield continuously decreases, showing a positive field response in the spin-polarized catalyst. The catalytic enhancement is consistent with a spin-associated contribution, although non-spin field effects should also be excluded before assigning the response exclusively to spin polarization. In addition, Co doping also modifies the band structure, built-in electric field, and charge separation efficiency, which may contribute to the enhanced performance together with the spin polarization. Liu et al. [90] also investigated the synergistic effect between doping and magnetic field application in the Co-doped $BiVO_4$ system. It is found that the spin-up and spin-down DOS of 2Co-$BiVO_4$ exhibit pronounced asymmetry, indicating that Co doping induces spin polarization. Under a 100 mT external magnetic field, the enhancement of yield over time for 2Co-$BiVO_4$ is significantly greater than that without the magnetic field, indicating that the field-responsive catalyst exhibits changes consistent with a spin contribution, while additional transport effects may coexist. Karbalaei Akbari et al. [91] also investigated the synergistic effect between doping and an external magnetic field in the Ga-Gd oxide nanocomposite system. According to the $^{71}$Ga free induction decay (FID) curves (Figure 5a), the signal decay of the Gd-containing sample is significantly faster than that of the Gd-free sample, indicating that the introduction of Gd forms local magnetic moments and endows the material with magnetic responsiveness. The magnetic response intensity versus potential curves in Figure 5b show a distinct response peak near −0.55 V, and the magnetic response increase is driven by the magnetic-field strength, indicating that the magnetic field selectively enhances $CO_2$RR without significantly affecting other electrochemical processes. For the annealed Ga-Gd sample under a 200 mT magnetic field, the CO production rate increases from 0.22 mmol $g^{-1}$ $h^{-1}$ to approximately 0.42 mmol $g^{-1}$ $h^{-1}$, and the $CH_3OH$ production rate increases from approximately 0.06 mmol $g^{-1}$ $h^{-1}$ to approximately 0.18 mmol $g^{-1}$ $h^{-1}$. In contrast, samples without annealing or without Gd doping show no significant magnetic enhancement. Lin et al. [71] also observed the synergistic effect between doping and an external magnetic field in Mn-doped $CsPbBr_3$ nanoplatelets. EPR spectra reveal that pristine $CsPbBr_3$ shows no signal, whereas Mn-$CsPbBr_3$ exhibits a distinct EPR signal, indicating that $Mn^{2+}$ doping introduces unpaired electrons and generates spin polarization. As shown in Figure 5c, the CO yield of Mn-$CsPbBr_3$ increases significantly with increasing magnetic-field strength, reaching 105.7 μmol $g^{-1}$ at 300 mT, which is 2.3 times that when no magnetic field is applied. The $CH_4$ yield also increases from 3.5 to 4.8 μmol $g^{-1}$. A comparison shows that only the Mn-doped sample exhibits magnetic field responsiveness, indicating that Mn doping is a prerequisite for the magnetic field response, and the external magnetic field further enhances the product yields on this basis.

The absence of a comparable response in the undoped control strengthens the spin-related interpretation for this system, although the broader distinction between spin-associated and non-spin magnetic-field effects will be discussed in Section 3.4.

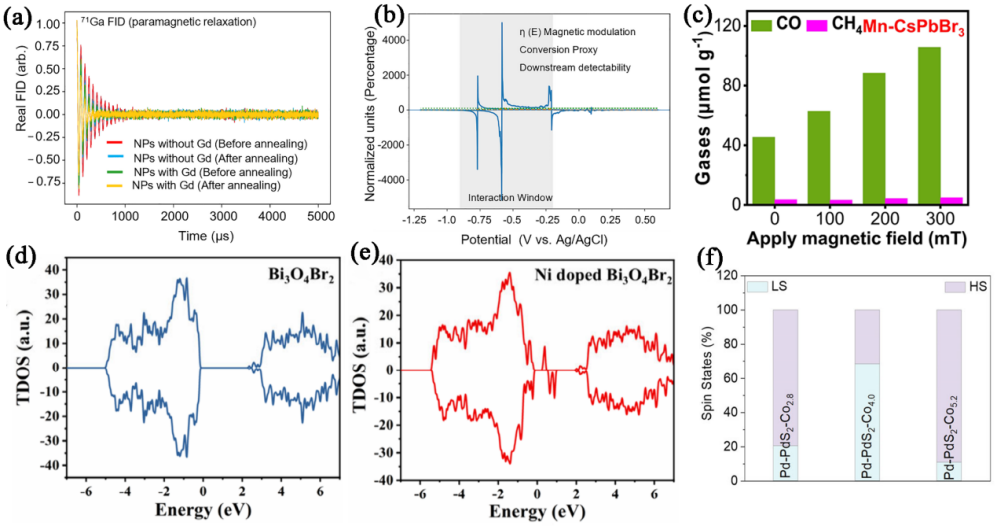



**Figure 5.** (**a**) $^{71}$Ga free induction decay curves of Ga-Gd samples before and after annealing; (**b**) Potential-resolved magnetic response intensity curves of Ga-Gd before and after annealing under different magnetic-field strengths. (**a**,**b**) Reproduced with permission [91]. Copyright 2026, American Chemical Society; (**c**) $CO_2$ reduction product yields of Mn-$CsPbBr_3$ nanoplates under different external magnetic fields. (**c**) Reproduced with permission [71]. Copyright 2022, American Chemical Society; (**d**) DOS of undoped $Bi_4O_5Br_2$. (**e**) Total DOS of Ni-doped $Bi_4O_5Br_2$. (**d**,**e**) Reproduced with permission [92]. Copyright 2024, American Chemical Society; (**f**) Low-spin and high-spin percentage charts of $Co^{3+}$ in Pd-$PdS_2$-$Co_{2.8}$, Pd-$PdS_2$-$Co_{4.0}$, and Pd-$PdS_2$-$Co_{5.2}$. (**f**) Reproduced with permission [93]. Copyright 2025, Wiley-VCH GmbH.

### 3.1.3. Magnetic Modulation via Synergy Between Doping and Vacancies

The combination of atomic doping with vacancy defects can exploit the magnetic coupling effect between dopant atoms and the unpaired electrons around vacancies, thereby further amplifying spin polarization and modulating spin distribution. For semiconductors, the resulting spin polarization can contribute to suppressing carrier recombination, which in turn promotes charge carrier separation and enhances the overall catalytic performance of $CO_2$RR. Wang et al. [94] further verified the synergistic effect between doping and vacancies by simultaneously introducing oxygen vacancies into Co-doped $ZnSn(OH)_6$. Magnetization measurements reveal that the magnetization of 5CZSOH-$V_O$ is substantially higher than that of $ZnSn(OH)_6$, ZSOH-$V_O$ ($ZnSn(OH)_6$ with only oxygen vacancies), and 5CZSOH (Co-doped $ZnSn(OH)_6$ without oxygen vacancies), indicating that the synergistic effect between Co doping and oxygen vacancies significantly enhances spin polarization. DFT calculations confirm that the DOS of pristine $ZnSn(OH)_6$ is completely symmetric, whereas 5CZSOH-$V_O$ exhibits pronounced asymmetry between spin-up and spin-down channels, with spin polarization distributed across both Co and Sn atoms. The results of photocatalytic $CO_2$ reduction show that the CO yield of 5CZSOH-$V_O$ reaches 204.10 μmol $g^{-1}$ $h^{-1}$, which is 15.14 times, 12.93 times, and 4.93 times that of $ZnSn(OH)_6$, ZSOH-$V_O$, and 5CZSOH, respectively. These results suggest that the enhanced $CO_2$RR performance may arise from the combined effects of spin polarization and the strengthened full-space electric field, together with other Co-doping and vacancy-induced changes in band structure, charge distribution, and carrier separation. Wang et al. [95] constructed atomic-scale Cu-$V_O$-Ti redox sites by doping Cu into $TiO_2$ and introducing oxygen vacancies. DFT calculations reveal that pristine $TiO_2$ exhibits symmetric spin-up and spin-down states near the Fermi

level, indicating the absence of spin polarization. In contrast, the introduction of Cu significantly breaks this symmetry, with the spin-up state density being much higher than the spin-down state, thereby generating pronounced spin polarization. This spin polarization suppresses electron–hole recombination and promotes charge separation. The results of photocatalytic $CO_2$ reduction show that under 15% low-concentration $CO_2$, the main product of pristine $TiO_2$ is CO, with a $CH_4$ yield of only 0.58 μmol $g^{-1}$ $h^{-1}$. Upon introducing Cu and oxygen vacancies, the $CH_4$ yield of the TC-2 sample significantly increases to 25.87 μmol $g^{-1}$ $h^{-1}$, while the CO yield notably decreases. This indicates that the synergy between Cu doping and oxygen vacancies alters the reaction pathway, enabling highly selective conversion from CO to $CH_4$. At the same time, Cu doping and oxygen vacancies also introduce defect states, modify the local coordination and band structure, create adjacent Cu-$V_O$-Ti redox sites, and affect $CO_2$ adsorption and intermediate energetics, which may also contribute to the enhanced $CH_4$ selectivity. Wang et al. [96] investigated the modulation of $CO_2$RR performance on transition metal (Fe, Co, Mo) SAC supported on hexagonal boron nitride (h-BN) with adjacent monovacancies through theoretical calculations. It is found that there exists a volcano-type relationship between the CO adsorption energy and the $CO_2$RR overpotential, with the volcano peak located at −1.13 eV, indicating that a moderate CO adsorption strength is favorable for attaining optimum catalytic activity. Among them, Co-$B_2$@BN and Fe-$B_3$@BN are located near the volcano peak, with overpotentials of 0.28 V and 0.32 V, respectively. Further analysis reveals that spin polarization is closely correlated with the M-C bond strength. For the Co-vac@BN and Mo-vac@BN systems, the integrated projected crystal orbital Hamiltonian population (IpCOHP) of the M-C bond generally exhibits a declining trend with the spin splitting of the *d*-band center ($\Delta\varepsilon_d$) of the metal atoms.

#### 3.1.4. Magnetic Modulation via Synergy Between Doping and Heterojunctions

In addition to constructing vacancy defects within a single material, extending doping to heterojunction interfaces and exploiting magnetic exchange coupling between different materials along with the interfacial built-in electric field can further enrich the degrees of freedom for magnetic modulation. By performing atomic doping on one or both sides of the heterojunction, the doping-induced spin polarization can synergize with the charge transfer and built-in electric field at the heterojunction interface, thereby achieving more efficient charge carrier separation and improved $CO_2$RR performance. Zhao et al. [97] constructed a Z-scheme heterojunction Mn-CPB/ZnPc by combining $Mn^{2+}$-doped $CsPbBr_3$ nanoplatelets with ZnPc, achieving synergy between spin polarization and interfacial charge transfer. PL spectra reveal that the PL intensity of Mn-CPB/ZnPc is much lower than that of CPB and Mn-CPB, indicating that the heterojunction effectively suppresses radiative recombination. Time-resolved photoluminescence (TRPL) results show that the $Mn^{2+}$ emission lifetime of Mn-CPB is 0.20 ms, whereas that of Mn-CPB/ZnPc is shortened to 0.16 ms. Meanwhile, the exciton decay lifetime decreases from 3.06 ns for Mn-CPB to 1.79 ns for Mn-CPB/ZnPc. The photocatalytic $CO_2$ reduction performance data show that the CO yield of Mn-CPB/ZnPc reaches 15.17 μmol $g^{-1}$ $h^{-1}$, which is 3.7 times and 5 times that of CPB and ZnPc, respectively, while the $CH_4$ yield is also significantly enhanced. This observation is consistent with a synergistic effect between Mn doping-induced spin polarization and the Z-scheme heterojunction, which significantly enhances the $CO_2$ reduction performance. Yang et al. [92] constructed a heterojunction of Ni-doped $Bi_4O_5Br_2$ with $NiCo_2O_4$. As shown in the DOS plots in Figure 5d, the DOS of undoped $Bi_4O_5Br_2$ is completely symmetric, whereas that of Ni-doped $Bi_4O_5Br_2$ (Figure 5e) exhibits asymmetric spin-up and spin-down DOS near the Fermi level, indicating that Ni doping induces spin polarization. The chronoamperometric (i-t) response shows that the photocurrent density of 21N-BON is

significantly higher than that of BON and NCO, indicating that the heterojunction improves the separation efficiency of photogenerated charge carriers. Photocatalytic $CO_2$ reduction performance data reveal that the CO yield of 21N-BON is significantly superior to that of the other catalysts. This indicates that the synergy between Ni doping-induced spin polarization and the built-in electric field at the heterojunction significantly enhances the $CO_2$ reduction performance. In addition, Liu et al. [93] further revealed the modulating effect of the $Co^{3+}$ spin state on the Pd electronic structure by constructing a Pd-$PdS_2$-$Co_x$ heterojunction. As shown in Figure 5f, the spin-state proportion diagram indicates that the low-spin proportions of $Co^{3+}$ in Pd-$PdS_2$-$Co_{2.8}$, Pd-$PdS_2$-$Co_{4.0}$, and Pd-$PdS_2$-$Co_{5.2}$ are 20.6%, 68.4%, and 10.9%, respectively, while the high-spin proportions are 79.4%, 31.6%, and 89.1%, respectively, indicating that the $Co_{4.0}$ sample predominantly adopts a low-spin configuration. When Pd-$PdS_2$-$Co_{4.0}$ was employed as the anode in the coupled glycerol oxidation and $CO_2$ reduction system, the anodic HCOOH FE approached 90%. This work focuses on the anodic glycerol oxidation in a coupled system, rather than providing direct evidence for cathodic $CO_2$RR spin effects.

### *3.2. Magnetic Modulation via Axial Coordination*

Axial coordination can effectively regulate the performance of $CO_2$RR by introducing additional ligands along the axial orientation of the active metal center, which breaks the original symmetry of the planar configuration, induces *d*-orbital energy-level splitting and electron rearrangement, and consequently optimizes the binding strength of key intermediates [98,99]. Beyond these electronic effects, axial coordination also offers a unique opportunity to modulate the spin configuration of the metal site, which provides an additional avenue for tuning the catalytic behavior. This section focuses on the magnetic aspect of axial coordination and its impact on $CO_2$RR. Introducing additional ligands in the axial direction of the active metal center can effectively break the original symmetry of the planar configuration, induce *d*-orbital energy-level splitting and electron rearrangement, and consequently alter the spin state of the metal site. This axial coordination strategy directly modulates the electronic structure through ligands, independent of lattice doping or external physical fields, offering a novel strategy for the precise design of $CO_2$RR catalysts. Miao et al. [27] successfully constructed a NiP-$N_4$-C SAC by coordinating a P atom located at the axial position of the Ni-$N_4$ plane, thereby modulating the spin state of the Ni single atom. The EPR spectra in Figure 6a reveal that no signal is detected for Ni-$N_4$-C, whereas NiP-$N_4$-C exhibits a distinct EPR signal at 3000 G, indicating that axial P coordination generates unpaired electrons at the Ni center and induces the spin state to evolve from low-spin to high-spin. Free energy diagrams reveal that the uphill free energy of *COOH on NiP-$N_4$-C is lower than that on Ni-$N_4$-C by 1.36 eV, indicating that the unpaired *d* electrons of Ni in the high-spin state enhance the *d*-*p* orbital coupling with *COOH, which may contribute to lowering the thermodynamic requirement of the PDS. Sun et al. [60] introduced an O bridge bond along the axial direction of the Fe-$N_4$ plane to construct an O-Fe-$N_4$ SAC, achieving spin-state modulation of the Fe single atom. The $1/\chi$-T curves in Figure 6b reveals that the unpaired electron count of Fe in Fe-$N_4$ is 2, whereas that in O-Fe-$N_4$ after axial O coordination increases to 5, indicating that Fe transitions from an intermediate-spin state to a high-spin state. The corresponding free energy diagrams (Figure 6c) show that the uphill free energy of *COOH on Fe-$N_4$ is 0.94 eV, whereas that on O-Fe-$N_4$ is reduced to 0.72 eV. Wei et al. [100] elucidated the role of axial O coordination on the electrocatalytic $CO_2$ reduction performance of the Ni-$N_4$-C SAC through DFT calculations. The O atoms on the MXene surface form an axial Ni-O coordination bond with the Ni center, shortening the Ni-O distance to 2.34 Å and inducing a charge transfer of approximately 0.11 electrons. Unlike the uncoupled Ni-$N_4$ sites, which exhibit no spin

polarization, the newly formed Ni-$N_4O$ configuration removes the spin-state degeneracy of the Ni *d* orbitals, with the spin-down *d*-orbital energy levels shifting significantly upward. The *d* electrons are redistributed between the spin-up and spin-down channels, generating a net spin moment of approximately 1.4 μB on Ni (Figure 6d) and substantially reducing the free energy requirement for *COOH formation. The corresponding free energy diagrams (Figure 6e) show that the free energy requirement for *COOH on pristine Ni-$N_4$-C is 1.76 eV, whereas that on the $Hf_3C_2$-coupled system is reduced to 1.01 eV. Spin polarization reduces the occupation of certain *d* orbitals of Ni, weakening the occupation of the *d*-$\pi$ antibonding orbitals between Ni and *COOH, thereby significantly stabilizing the *COOH intermediate. Zhang et al. [67] loaded Ni and Mn ions into the pores of different ZIF-8 crystals using a dual-solvent method, and after pyrolysis, prepared a DAC with an axial coordination structure. In the Ni-Mn DAC, the axial Ni atom is connected to the in-plane Mn-$N_3$ site through a C-Ni-N-Mn-$N_3$ coordination pathway. Extended X-ray absorption fine structure (EXAFS) fitting reveals that the Ni atom exhibits two scattering paths, namely Ni-C and Ni-N, which have coordination numbers of 1.1 and 1.2, respectively, confirming the axial C-Ni-N configuration. Vibrating sample magnetometry (VSM) and superconducting quantum interference device (SQUID) measurements show that in the Mn-$N_3$ SAC, the number of unpaired electrons of Mn is approximately 1, with a low effective magnetic moment, corresponding to a low-spin state. In the Ni-Mn DAC, the number of unpaired electrons of Mn increases to 3, coupled with a rise in the effective magnetic moment, suggesting a transition to a high-spin state. As shown in Figure 6f, the *d*-band center of high-spin Mn shifts upward from −2.45 eV in Mn-$N_3$ to −2.13 eV, enhancing the adsorption of *CO. Consequently, CO undergoes further hydrogenation to $CH_4$ on the Ni-Mn catalyst, with a $CH_4$ FE of 11.4%.

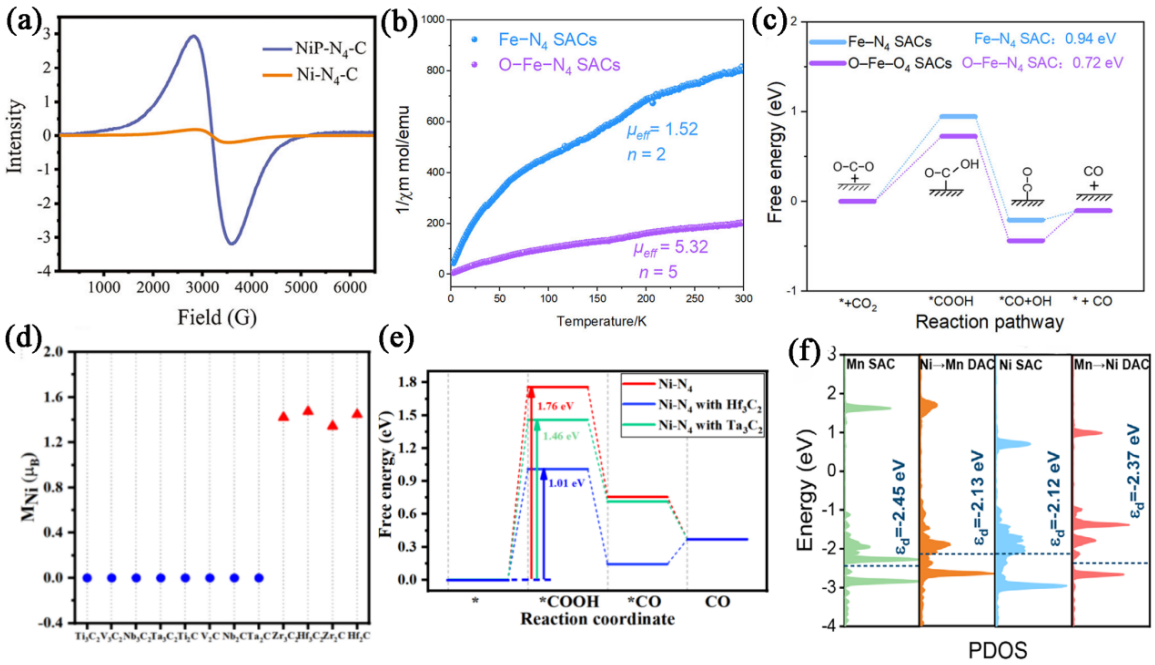



**Figure 6.** (**a**) EPR spectra of NiP-$N_4$-C and Ni-$N_4$-C. (**a**) Reproduced with permission [27]. Copyright 2024, Wiley-VCH GmbH; (**b**) 1/χ-T curves of Fe-$N_4$ and O-Fe-$N_4$. (**c**) Free energy diagrams of $CO_2$RR on Fe-$N_4$ and O-Fe-$N_4$ SACs. (**b**,**c**) Reproduced with permission [60]. Copyright 2026, Wiley-VCH GmbH; (**d**) Comparison of spin magnetic moments of Ni atoms in Ni-$N_4$-C with different MXene substrates. (**e**) Free energy diagrams of $CO_2$RR on pristine Ni-$N_4$-C and Ni-$N_4$-C coupled with $Hf_3C_2$ and $Ta_3C_2$. (**d**,**e**) Reproduced with permission [100]. Copyright 2026, American Chemical Society; (**f**) Comparison of *d*-band centers of Ni-Mn DAC and Mn SAC. (**f**) Reproduced with permission [67]. Copyright 2025, Wiley-VCH GmbH. * stands for the adsorption site at the surface of catalyst.

### *3.3. Magnetic Modulation via Defect Engineering*

Defect engineering modulates the catalytic performance of $CO_2$RR by creating additional active sites, tuning the coordination environment, and introducing localized electronic states that facilitate $CO_2$ activation and intermediate conversion [101–103]. Beyond these effects, defect engineering can also induce spin polarization and alter local magnetic moments by modulating the coordination configuration and electronic configuration of active centers. The resulting modulation of intrinsic magnetic moments can significantly influence the adsorption characteristics of intermediates and the reaction free energy requirements during $CO_2$RR, providing an additional route for performance enhancement. Wang et al. [51] used intrinsically ferromagnetic $Fe_3GeTe_2$ as a model system and activated $CO_2$ by constructing single Te vacancies. As shown in Figure 7a, pristine $Fe_3GeTe_2$ exhibits pronounced spin polarization near the Fermi level with asymmetric spin-up and spin-down DOS, while after introducing Te vacancies, the DOS in the spin-down channel is significantly enhanced, indicating that defect engineering further strengthens spin polarization. The results show that the introduction of Te vacancies enhances the local magnetic moments of Fe atoms, and these magnetic moments exhibit a highly linear correlation with the *d*-band center. DFT-based free energy calculations further reveal (Figure 7b) that when the magnetic moment is tuned to the optimal value of 1.2 μB, the overpotential of the PDS is as low as −0.46 V, and the selectivity for $CH_4$ formation is superior to that of the HER. Further analysis reveals that magnetic moments that are too large or too small deviate from the optimal adsorption energy corresponding to the volcano peak, thereby reducing the activity and exhibiting a typical volcano-shaped relationship, supporting a strong correlation between intrinsic magnetic moment and catalytic performance. Jin et al. [104] used ZnTCPP ultrathin nanosheets as a photocatalyst and introduced N vacancies into the organic framework via $N_2$ plasma treatment. EPR spectra and DFT calculations show that the N vacancies (NVs) induce pronounced electron spin polarization and generate defect levels, narrowing the bandgap from 1.9 eV to 1.8 eV and shifting the CBM from −0.83 eV to −1.08 eV. The spin-up and spin-down density of states of ZnTCPP near the Fermi level are largely symmetric, whereas after introducing N vacancies, the spin density of states of NVs-ZnTCPP exhibits pronounced asymmetry with the spin-down channel significantly enhanced, indicating the generation of spin polarization. The induced spin polarization is considered to contribute to suppressing photogenerated charge carrier recombination, and both chronoamperometric i-t and PL quenching experiments confirm higher charge separation efficiency. Meanwhile, DFT calculations further reveal that the formation free energy of *COOH in the PDS decreases from 1.98 eV to 0.95 eV, ultimately increasing the CO yield by a factor of 2.7 and enhancing the CO selectivity from 60.9% to 79.6%. Overall, the enhanced photocatalytic performance may arise from the combined effects of spin polarization, defect-level formation, and band-structure modification.

### *3.4. Direct Modulation by External Magnetic Field*

An external magnetic field can influence $CO_2$RR through more than one physical pathway. In magnetic catalysts, the field may reorganize magnetic domains, change magnetic moments, modify spin polarization, and perturb spin-dependent bonding. In contrast to strategies that rely on the design of intrinsic material structures, directly applying an external magnetic field to the catalytic system offers operational simplicity and enables dynamic regulation during the reaction [40,58,68,105]. Wei et al. [105] systematically investigated the modulating effect of an external magnetic field on the $CO_2$RR performance of Ni-based magnetic catalysts. It is found that at different potentials, the CO FE increases significantly in the presence of a 320 mT magnetic field, returns to its original value upon removal of the field, and exhibits consistent behavior over multiple cycles, indicating that the magnetic

field reversibly enhances CO selectivity. Magnetization measurements reveal that the catalyst exhibits typical soft ferromagnetic properties, with high sensitivity to external magnetic fields and the ability to achieve aligned magnetic moments at relatively low field strengths. It has been further reported that an increase in the magnetic-field strength correlates with changes in charge-transfer resistance and current density. More importantly, the magnetic field also affects the chemical bonding of reaction intermediates. Operando attenuated total reflection surface-enhanced infrared absorption spectroscopy (ATR-SEIRAS) analysis shows that upon application of the magnetic field, the C-O stretching vibration peak of the *COOH intermediate redshifts from 1235 $cm^{-1}$ to 1223 $cm^{-1}$, indicating a change in the bonding environment of the intermediate under the field. Zhu et al. [58] directly observed the modulation of magnetic domains by an external magnetic field using quantum diamond atomic force microscopy (QDAFM). Magnetic hysteresis loop analysis reveals that Ni@NC exhibits typical soft ferromagnetic properties with a low coercivity, indicating high sensitivity to external magnetic fields. The QDAFM images in Figure 7c reveal that in the absence of a magnetic field, the catalyst surface exhibits mixed magnetic domains separated by domain walls. Upon application of a 140 mT magnetic field, the domain walls disappear and the entire region transforms into a uniformly magnetized single domain. This magnetic domain reconstruction significantly boosts the $CO_2$ reduction activity. Upon application of the magnetic field, the CO FE approaches 100% over the potential range from −0.3 V to −1.1 V. In addition, Yin et al. [68] investigated the influence of an AMF on $CO_2$RR. Under the AMF at a frequency of 500 kHz, infrared thermal imaging shows that the catalyst surface temperature increases by only approximately 7 °C. The i-t curves in Figure 7d show that when the AMF is periodically switched on and off, the current response of the catalyst at −0.2 V is significantly enhanced and rapidly returns to its original level upon turning off the AMF. Meanwhile, the CO FE under AMF reaches as high as 94.5%, whereas it is significantly lower in the absence of the magnetic field (Figure 7e). In the $H_2O$/deuterium oxide ($D_2O$) comparative experiments, the kinetic isotope effect (KIE) is 5.5 in the absence of a magnetic field and decreases to 2.1 upon application of the magnetic field, indicating an influence on proton-transfer behavior, but the thermal and transport contributions should be considered together with any spin interpretation. Song et al. [40] placed the catalyst in a tunable magnetic field with intensities ranging from 0 to 3 T and performed $CO_2$RR in acidic electrolyte. The temperature-dependent inverse magnetic susceptibility ($\chi^{-1}$-T) curves of the catalyst were measured with and without an external magnetic field. Upon application of a 2 T magnetic field, the effective magnetic moment increases from 0.47 μB to 2.72 μB. Furthermore, the free energy diagrams obtained from DFT calculations (Figure 7f) show that as the magnetic moment increases, the free energy of the PDS for $CO_2$RR decreases successively from 0.80 eV to 0.64 eV and then to 0.45 eV. Meanwhile, the adsorption free energy of *H for the competing HER increases from 0.76 eV to 0.85 eV.

At the same time, an external field can alter the transport of charged species through Lorentz-force and magnetohydrodynamic effects, change interfacial mass transfer, and in alternating fields introduce thermal contributions. These effects can coexist and should be separated experimentally whenever possible [106,107]. A change in current density, FE, or product distribution under an external magnetic field is evidence of a field response but is not, by itself, proof of a spin-mediated catalytic mechanism. Spin-associated interpretations are strengthened when catalytic changes are accompanied by direct magnetic or spin characterization, such as EPR, XMCD, VSM/SQUID measurements, spin-resolved spectroscopy, or real-space magnetic-domain imaging. Calculated spin densities and spin-resolved DOS can support an electronic-structure hypothesis, but they do not independently establish the dominant experimental mechanism. Conversely, field-orientation dependence,

current-density dependence, stirring or flow controls, nonmagnetic catalyst controls, and constant-temperature experiments are particularly useful for evaluating Lorentz-force, magnetohydrodynamic, mass-transfer, and thermal contributions. A useful example of a non-spin pathway is the imidazolium-assisted $CO_2$RR system [106], where the magnetic-field-dependent selectivity was attributed to enhanced transport of charged $CO_2$ complexes through the Lorentz force rather than to a change in the catalyst spin state. Such examples are important controls for the broader literature because they show that magnetic-field responsiveness and spin regulation are related but not synonymous concepts. Future studies should therefore combine magnetic characterization with electrochemical controls under matched potential, pH, temperature, electrolyte, and mass-transfer conditions before assigning a catalytic enhancement primarily to spin polarization.

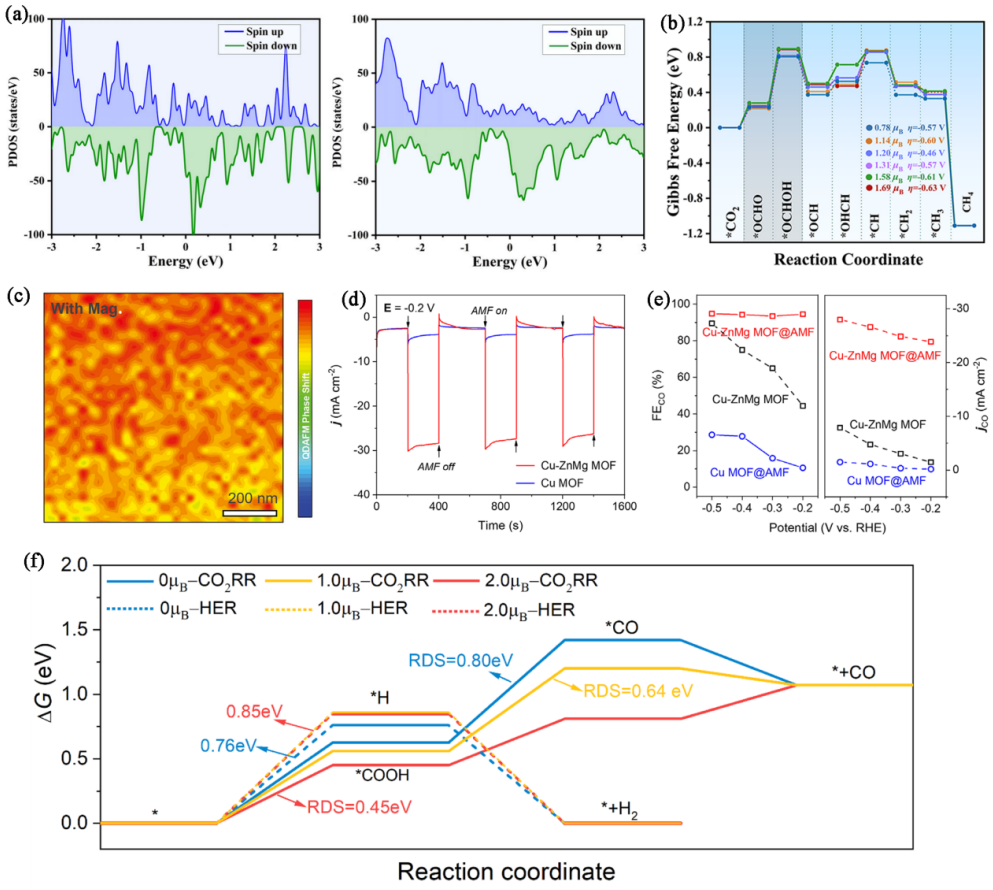



**Figure 7.** (**a**) PDOS of pristine $Fe_3GeTe_2$ monolayer and $Fe_3GeTe_2$ with Te vacancy; (**b**) Free energy diagrams of $CO_2$RR on defective $Fe_3GeTe_2$ under different magnetic moments. (**a**,**b**) Reproduced with permission [51]. Copyright 2025, American Chemical Society; (**c**) QDAFM images of the magnetic domain structure of Ni@NC with and without a magnetic field. (**c**) Reproduced with permission [58]. Copyright 2024, Wiley-VCH GmbH; (**d**) i-t curves under periodic on-off AMF. (**e**) CO FE with and without AMF. (**d**,**e**) Reproduced with permission [68]. Copyright 2025, Wiley-VCH GmbH; (**f**) Free energy diagrams of $CO_2$RR and HER on Ni-$N_5$-C under different atomic spin magnetic moments. (**f**) Reproduced with permission [40]. Copyright 2025, American Chemical Society. * stands for the adsorption site at the surface of catalyst.

## 4. Conclusions and Outlook

Although magnetic regulation has demonstrated considerable potential in $CO_2$RR, current studies rely on static or ex situ characterization and often evaluate magnetic effects under electrochemical conditions that differ in potential, pH, electrolyte, temperature, or mass transport. A key future challenge is therefore to connect operando magnetic descrip-

tors with reaction conditions and catalytic observables while separating spin-associated effects from other field-induced contributions. Machine learning (ML), artificial intelligence (AI), and advanced sensing technologies can support this goal by integrating magnetic, structural, electrochemical, and dynamic information into more interpretable models and experimental workflows.

### *4.1. ML for Catalyst Screening and Performance Prediction*

Traditional approaches struggle to handle the complex combinatorial relationships among numerous variables such as catalyst composition, spin states, magnetic moments, and defect types. ML can establish predictive models from material features to catalyst performance by training on experimental and computational data, enabling rapid evaluation of electronic structure properties, intermediate adsorption free energies, and product selectivity of a large number of candidate materials [108–111]. For magnetic $CO_2$RR, physically meaningful descriptors should extend beyond composition to include magnetic moment, spin state, spin-resolved *d*-band centers, *p*-band descriptors, coordination, strain, potential, pH, electrolyte identity, field strength, field orientation, and field frequency. These variables can be incorporated as explicit features or physical constraints to improve interpretability and transferability. ML potentials provide a complementary route by enabling larger-scale simulations of dynamic interfaces and surface reconstruction. A recent pH-dependent $CO_2$RR study on Sn-based catalysts combined an MLP with molecular dynamics and pH-field-coupled microkinetic modeling, illustrating how operating conditions can be incorporated into data-driven mechanistic analysis [112]. Active learning can then prioritize uncertain or promising candidates for additional DFT calculations or experiments rather than relying on exhaustive screening.

### *4.2. AI for Multi-Physics Simulation and Pathway Discovery*

$CO_2$RR under magnetic regulation involves coupled magnetic, electronic, structural, and electrochemical variables. Conventional ML screening generally maps predefined descriptors to target properties and ranks candidate catalysts, whereas physics-informed models additionally embed physical descriptors or constraints associated with spin states, adsorption, charge transfer, and operating conditions. ML potentials can extend this framework to dynamic structures and larger simulation cells. AI-agent-driven discovery represents a further level of automation in which candidate generation, DFT or MLP evaluation, uncertainty analysis, data interpretation, and experimental selection are linked iteratively. A practical closed-loop workflow would proceed from candidate generation to DFT/MLP prediction, targeted experimental validation, operando magnetic characterization, data feedback, and model updating [113]. Such a workflow is more demanding than conventional ML screening but may be particularly useful for magnetic $CO_2$RR because catalyst structure, spin state, and reaction environment can evolve together under operating conditions.

### *4.3. Sensors for In Situ Magnetic Monitoring and Real-Time Feedback Control*

During $CO_2$RR, spin states, oxidation states, and magnetic-domain structures can evolve with applied potential, adsorbate coverage, and external magnetic fields. Future studies should therefore prioritize operando or in situ approaches capable of tracking these changes during catalysis. In situ EPR has already been used to visualize dynamic electronic-state evolution during photocatalytic $CO_2$ reduction [114]. Related real-time interfacial tracking methods developed in other electrochemical systems can serve as methodological inspiration [115], but they should not be treated as direct evidence for magnetic $CO_2$RR. Integrating magnetic characterization with spectroscopy, electrochemical measurements, and local temperature or transport monitoring would make it possible to

correlate spin-state transitions with reaction intermediates and catalytic responses while testing alternative non-spin explanations. These data could ultimately feed into closed-loop control strategies in which the magnetic field or electrode potential is adjusted on the basis of operando observables.

In summary, magnetic modulation provides an additional degree of freedom for regulating $CO_2$ reduction through changes in spin state, magnetic moment, spin-resolved electronic structure, and magnetic-domain organization. These variables can modify intermediate adsorption and reaction thermodynamics, but their catalytic consequences depend strongly on the local coordination environment and electrochemical conditions. External magnetic fields require particularly careful interpretation because spin-associated changes can coexist with Lorentz-force-driven transport, magnetohydrodynamic convection, thermal effects, and interfacial mass-transfer changes. Accordingly, future work should combine direct magnetic characterization with matched electrochemical controls before assigning field-enhanced activity or selectivity primarily to spin polarization. At the catalyst-design level, doping, axial coordination, vacancies, heterojunctions, and molecular frameworks provide complementary routes for controlling magnetic and electronic structures. Integrating these descriptors with operando characterization, physics-informed ML, ML potentials, and iterative AI-assisted workflows may enable more reliable identification of the relationships among magnetic properties, reaction pathways, and product selectivity.

**Author Contributions:** Investigation, D.Z., S.X. and C.M.; data curation, D.Z., M.B., H.F. and L.J.; writing—original draft preparation, D.Z., S.X. and L.J.; writing—review and editing, M.B., H.F. and L.J.; visualization, S.X. and C.M.; supervision, L.J.; project administration, L.J.; funding acquisition, C.M., H.F. and L.J. All authors have read and agreed to the published version of the manuscript.

**Funding:** This work is funded by the National Natural Science Foundation of China (Grant No. 22573002), the Program for Science & Technology Innovation Talents in Universities of Henan Province (Grant No. 24HASTIT013), the Science and Technology Research Project of Henan Province (Grant No. 262102231008), and the College Students Innovation Fund of Anyang Normal University (Grant No. 202610479092).

**Data Availability Statement:** No new data were created or analyzed in this study. Data sharing is not applicable to this article.

**Acknowledgments:** We thank the Computational Laboratory for Energy Conversion and Storage for the support.

**Conflicts of Interest:** The authors declare no conflict of interest.

## References

1. Zuo, C.; Su, Q.; Yan, X. Research Progress of Co-Catalysts in Photocatalytic $CO_2$ Reduction: A Review of Developments, Opportunities, and Directions. *Processes* **2023**, *11*, 867. [CrossRef]
2. Lu, H.; Fu, D.; Tai, X.; Sun, Z.; Wang, X. Metal–Organic Frameworks/Covalent–Organic Frameworks-Based Materials in Organic/inorganic Pollutant Elimination and $CO_2$ Reduction Applications. *ChemNanoMat* **2025**, *11*, e202500244. [CrossRef]
3. Chongdar, S.; Chatterjee, R.; Reza, S.; Pal, S.; Thapa, R.; Bal, R.; Bhaumik, A. Low Potential Electrochemical $CO_2$ Reduction to Methanol over Nickel-Based Hollow 0D Carbon Superstructure. *Adv. Energy Mater.* **2025**, *15*, 2403809. [CrossRef]
4. Xue, Q.; Qi, X.; Li, K.; Zeng, Y.; Xu, F.; Zhang, K.; Yang, T.; Qi, X.; Jiang, J. DFT Study of $CO_2$ Reduction Reaction to $CH_3OH$ on Low-Index Cu Surfaces. *Catalysts* **2023**, *13*, 722. [CrossRef]
5. Zhang, H.; Su, Q. Recent Advances of Indium-Based Sulfides in Photocatalytic $CO_2$ Reduction. *ACS Omega* **2025**, *10*, 8793–8815. [CrossRef] [PubMed]
6. Zuo, C.; Su, Q.; Jiang, Z. Advances in the Application of Bi-Based Compounds in Photocatalytic Reduction of $CO_2$. *Molecules* **2023**, *28*, 3982. [CrossRef] [PubMed]
7. Chen, L.; Chen, J.; Fu, W.; Chen, J.; Wang, D.; Xiao, Y.; Xi, S.; Ji, Y.; Wang, L. Energy-efficient $CO_2$ conversion to multicarbon products at high rates on CuGa bimetallic catalyst. *Nat. Commun.* **2024**, *15*, 7053. [CrossRef] [PubMed]

8. Li, Y.; Li, J.; Ai, W.; Chen, J.; Lu, T.; Liao, X.; Wang, W.; Huang, R.; Chen, Z.; Wu, J.; et al. Sequentially Regulating Potential-Determining Step for Lowering $CO_2$ Electroreduction Overpotential over Te-Doped Bi Nanotips. *Angew. Chem. Int. Ed.* **2024**, *63*, e202407772. [CrossRef] [PubMed]
9. Bai, Z.; Zhi, Z.; Jiang, X.Z.; Luo, K.H. Rational Design of Dual-Atom Catalysts for Electrochemical $CO_2$ Reduction to $C_1$ and $C_2$ Products with High Activity and Selectivity: A Density Functional Theory Study. *Ind. Eng. Chem. Res.* **2025**, *64*, 4378–4387. [CrossRef] [PubMed]
10. Khalil, M.; Kadja, G.T.M.; Nugroho, F.A.A.; Sutanto, L.G.; Jiwanti, P.K.; Abdi, F.F.; Hussin, F.; Aroua, M.K. Suppressing the competing hydrogen evolution reaction in $CO_2$ electroreduction: A review. *Renew. Sust. Energy Rev.* **2024**, *206*, 114869. [CrossRef]
11. Deng, B.; Sun, D.; Zhao, X.; Wang, L.; Ma, F.; Li, Y.; Dong, F. Accelerating acidic $CO_2$ electroreduction: Strategies beyond catalysts. *Chem. Sci.* **2024**, *15*, 15087–15108. [CrossRef] [PubMed]
12. Ou, L. Competition between Initial $CO_2$ Electroreduction and Hydrogen Evolution Reaction on Cu Catalysts in Acidic Media: Role of Specifically Adsorbed Halide Anions. *Langmuir* **2024**, *40*, 13060–13069. [CrossRef] [PubMed]
13. Tafazoli, S.; Şekercioğlu, A.; Zarenezhad, H.; Ataş, B.; Mohammadpour, A.; Balkan, T.; Kaya, S. Cations Responsible for Varied $CO_2$RR Product Selectivity at High Overpotentials over $Cu_2O$ Nanocubes. *ACS Appl. Mater. Interfaces* **2025**, *17*, 50676–50685. [CrossRef] [PubMed]
14. He, T.; Sun, R.; Shi, R.; Chen, X.; Zhou, T.; Han, Y.; Liu, F.; Cui, H.; Li, H.; Liu, Q. From Dopant Periodicity to Asymmetric Sites: Steering C horizontal line C Coupling in Single-Atom Alloy Catalysts for Electrochemical $CO_2$ Reduction. *Angew. Chem. Int. Ed.* **2026**, *65*, e20426. [CrossRef] [PubMed]
15. Gong, S.; Zhai, Y.; Jin, C.; Xu, H.; Xia, Q.; Li, W.; Ying, Y.; Wu, J.; She, X.; Wang, Z.; et al. Interface engineering of single-molecular heterojunction catalysts for $CO_2$ electroreduction in strong acid medium. *Nat. Commun.* **2025**, *16*, 8704. [CrossRef] [PubMed]
16. Feldman, D.M.; Pellumbi, K.; Zimmermann, I.; Wiesner, W.; Sanden, S.A.; Suhr, S.C.B.; Holland, P.L.; Apfel, U.-P. Integrating salen complexes into gas diffusion electrodes for $CO_2$ electroreduction: Considerations for employing molecular precatalysts in heterogeneous electrolyzers. *Chem. Commun.* **2025**, *61*, 16974–16977. [CrossRef] [PubMed]
17. Zhu, X.; Zhou, E.; Tai, X.; Zong, H.; Yi, J.; Yuan, Z.; Zhao, X.; Huang, P.; Xu, H.; Jiang, Z. g-$C_3N_4$ S-Scheme Homojunction through Van der Waals Interface Regulation by Intrinsic Polymerization Tailoring for Enhanced Photocatalytic $H_2$ Evolution and $CO_2$ Reduction. *Angew. Chem. Int. Ed.* **2025**, *64*, e202425439. [CrossRef] [PubMed]
18. Zhu, X.; Zong, H.; Perez, C.J.V.; Miao, H.; Sun, W.; Yuan, Z.; Wang, S.; Zeng, G.; Xu, H.; Jiang, Z.; et al. Supercharged $CO_2$ Photothermal Catalytic Methanation: High Conversion, Rate, and Selectivity. *Angew. Chem. Int. Ed. Engl.* **2023**, *62*, e202218694. [CrossRef] [PubMed]
19. Wang, Y.; Liu, J.; Wang, Y.; Al-Enizi, A.M.; Zheng, G. Tuning of $CO_2$ Reduction Selectivity on Metal Electrocatalysts. *Small* **2017**, *13*, 1701809. [CrossRef] [PubMed]
20. Pan, F.; Zhang, H.; Liu, K.; Cullen, D.; More, K.; Wang, M.; Feng, Z.; Wang, G.; Wu, G.; Li, Y. Unveiling Active Sites of $CO_2$ Reduction on Nitrogen-Coordinated and Atomically Dispersed Iron and Cobalt Catalysts. *ACS Catal.* **2018**, *8*, 3116–3122. [CrossRef]
21. Wang, J.; Sun, M.; Xu, H.; Hao, F.; Wa, Q.; Su, J.; Zhou, J.; Wang, Y.; Yu, J.; Zhang, P.; et al. Coordination Environment Engineering of Metal Centers in Coordination Polymers for Selective Carbon Dioxide Electroreduction toward Multicarbon Products. *ACS Nano* **2024**, *18*, 7192–7203. [CrossRef] [PubMed]
22. Zhan, Q.-N.; Shuai, T.-Y.; Xu, H.-M.; Zhang, Z.-J.; Li, G.-R. Recent advances in the regulation of the coordination structures and environment of single-atom catalysts for carbon dioxide reduction reaction. *J. Mater. Chem. A* **2023**, *11*, 7949–7986. [CrossRef]
23. Wang, M.; Kong, L.; Lu, X.; Wu, C.M.L. Coordination Environment Engineering to Regulate the Adsorption Strength of Intermediates in Single Atom Catalysts for High-performance $CO_2$ Reaction Reduction. *Small* **2024**, *20*, 2310339. [CrossRef] [PubMed]
24. Song, J.; Lei, X.; Mu, J.; Li, J.; Song, X.; Yan, L.; Ding, Y. Boron-Doped Nickel–Nitrogen–Carbon Single-Atom Catalyst for Boosting Electrochemical $CO_2$ Reduction. *Small* **2023**, *19*, 2305666. [CrossRef] [PubMed]
25. Tang, T.; Wang, Z.; Guan, J. Optimizing the Electrocatalytic Selectivity of Carbon Dioxide Reduction Reaction by Regulating the Electronic Structure of Single-Atom M-N-C Materials. *Adv. Funct. Mater.* **2022**, *32*, 2111504. [CrossRef]
26. Liu, T.; Xu, T.; Li, T.; Jing, Y. Selective $CO_2$ Reduction over γ-Graphyne Supported Single-Atom Catalysts: Crucial Role of Strain Regulation. *J. Am. Chem. Soc.* **2024**, *146*, 24133–24140. [CrossRef] [PubMed]
27. Miao, K.; Qin, J.; Lai, S.; Luo, M.; Kuchkaev, A.; Yakhvarov, D.; Kang, X. Spin Regulation of Nickel Single Atom Catalyst via Axial Phosphor-Coordination Achieves Near Unity CO Selectivity in Electrochemical $CO_2$ Reduction. *Adv. Funct. Mater.* **2024**, *35*, 2419989. [CrossRef]
28. Hou, P.; Huang, Y.; Ma, F.; Wei, X.; Du, R.; Zhu, G.; Zhang, J.; Wang, M. S and N coordinated single-atom catalysts for electrochemical $CO_2$ reduction with superior activity and selectivity. *Appl. Surf. Sci.* **2023**, *619*, 156747. [CrossRef]
29. Huang, K.; Li, R.; Qi, H.; Yang, S.; An, S.; Lian, C.; Xu, Q.; Liu, H.; Hu, J. Regulating Adsorption of Intermediates via the Sulfur Modulating Dual-Atomic Sites for Boosting $CO_2$RR. *ACS Catal.* **2024**, *14*, 8889–8898. [CrossRef]

30. Cao, S.; Zhou, S.; Chen, H.; Wei, S.; Liu, S.; Lin, X.; Chen, X.; Wang, Z.; Guo, W.; Lu, X. How can the Dual-atom Catalyst FeCo–NC Surpass Single-atom Catalysts Fe–NC/Co–NC in $CO_2$RR?—CO Intermediate Assisted Promotion via a Synergistic Effect. *Energy Environ. Mater.* **2022**, *6*, e12287. [CrossRef]
31. Yang, J.; Shen, Y.; Chen, B.; Wu, Q.; Liao, Y.; Zhou, L.; Luo, J.; Mao, X.; Guo, J.; Luo, B.; et al. Cu/Ni dual-atom catalysts with charge regulation: Boosting $CO_2$ electroreduction selectivity via site-specific O/C-terminal asymmetric adsorption. *Chin. Chem. Lett.* **2026**, *37*, 112638. [CrossRef]
32. Zhu, X.; An, X.; Yuan, C.; Ye, Y.; Wang, Z.; Zhu, W.; Ling, W.; Jiang, Y.; Xie, S.; Dai, S.; et al. Nearly 100% CO Selectivity for $CO_2$ Reduction via Synergistic Engineering of Heteronuclear CuCo Dual Atoms. *ACS Appl. Mater. Interfaces* **2025**, *17*, 25348–25357. [CrossRef] [PubMed]
33. Wang, J.; Zhu, Z.; Lin, Y.; Qi, X.; Li, Z.; Jiang, J.; Niu, X.; Chen, J.S.; Wu, R. Modulating surface zinc species via facet engineering for efficient electroreduction of $CO_2$ to CO. *Chem. Eng. J.* **2024**, *481*, 148730. [CrossRef]
34. Wang, Z.; Yang, J.; Yi, S.; Wu, Z.; Yang, X.; Zhang, Y.; Wang, H.; She, X.; Xu, H. Crystal facet engineering of $CeO_2$-supported Cu sites and efficient anodic coupling for enhanced electrocatalytic $CO_2$ reduction to $CH_4$. *Chem. Eng. Sci.* **2025**, *305*, 121095. [CrossRef]
35. Liu, S.; Ban, Y.; Liu, Y.; Zhang, J.; Duan, X.; Chen, C.; Wang, Y. Engineering Geometric Active Sites in Cobalt Spinel Oxides for Energy and Environmental Catalysis. *Rare Met.* **2026**, *45*, e70207. [CrossRef]
36. Zhang, Q.; Sun, M.; Yuan, C.-Y.; Sun, Q.-W.; Huang, B.; Dong, H.; Zhang, Y.-W. Strong Electronic Coupling Effects at the Heterojunction Interface of $SnO_2$ Nanodots and g-$C_3N_4$ for Enhanced $CO_2$ Electroreduction. *ACS Catal.* **2023**, *13*, 7055–7066. [CrossRef]
37. He, Q.; Ma, D.; Du, Y.; Huang, Q.; Ji, J.; Wang, X.; Ji, H.; Ma, W.; Zhao, J. An Atypical Heterojunction in Favor of Conversion of $CO_2$ and Sunlight into $C_2H_4$. *Adv. Sci.* **2025**, *12*, 2503336. [CrossRef] [PubMed]
38. Zhang, J.; Yan, D.; Ding, G.; Wang, X.; Li, C.; Zhong, S.; Yu, Y.; Shuai, L.; Liao, G. Dual Co Sites in n–n Type Heterojunction Enable Selective Electrochemical Co-Valorization of HMF and $CO_2$. *Ang. Chem.* **2025**, *137*, e202511448. [CrossRef]
39. Zuo, L.; Deng, Y.; Chen, L.; He, T.; Yang, J.; Zhang, J. Fundamental Insights into Photoelectrochemical Carbon Dioxide Reduction: Elucidating the Reaction Pathways. *ACS Catal.* **2024**, *14*, 16795–16833. [CrossRef]
40. Song, J.; He, D.; Ma, X.; Liu, P.; Guo, W.; Sun, R.; Li, F.; Zhong, Z.; Zhou, H.; Tang, J.; et al. Magnetic Field-Enhanced Acidic $CO_2$ Electroreduction Reaction on Single Nickel-Site Catalysts. *J. Am. Chem. Soc.* **2025**, *147*, 16198–16206. [CrossRef] [PubMed]
41. Deng, J.; Li, P.; Liu, S.; Fan, S.; Shen, Y.; Wang, M. Magnetic field effects on electrochemical $CO_2$ reduction at bismuth based electrocatalyst. *Mater. Today Phys.* **2025**, *55*, 101751. [CrossRef]
42. Zeng, Y.; Zhao, J.; Wang, S.; Wang, W.; Lu, Y.R.; Xi, S.; Xu, W.; Yoda, Y.; Masuda, R.; Li, X.; et al. Unraveling the Dynamic Low-Spin State Evolution of Single-Fe-Atom Sites for Efficient $CO_2$ Electroreduction. *J. Am. Chem. Soc.* **2025**, *147*, 42539–42548. [CrossRef] [PubMed]
43. Wang, F.; Su, Q.; Zhang, X.; Chen, A. Spin-State Regulation of Single-Atom Catalysts: From Quantum Mechanisms to Multidimensional Dynamic Regulation Strategies. *Adv. Funct. Mater.* **2025**, *36*, e18600. [CrossRef]
44. Liu, Y.; Ren, X.; Wang, J.; Wang, H.; Yin, Z.; Wang, Y.; Huang, W.; Hu, X.; Xu, Z.J.; Deng, Y. Spin-State Effect of Tetrahedron-Coordinated Single-Atom Catalysts on $CO_2$ Electroreduction. *J. Am. Chem. Soc.* **2025**, *147*, 20318–20328. [CrossRef] [PubMed]
45. Wang, R.; Zhang, D.; Frauenheim, T.; Li, S.; Kong, Q. Modulating $CO_2$ Electroreduction on Dual-Atom Catalysts through Orbital Interactions. *J. Phys. Chem. Lett.* **2026**, *17*, 5148–5155. [CrossRef] [PubMed]
46. Wang, Y.; Sun, J.; Sun, N.; Zhang, M.; Liu, X.; Zhang, A.; Wang, L. The spin polarization strategy regulates heterogeneous catalytic activity performance: From fundamentals to applications. *Chem. Commun.* **2024**, *60*, 7397–7413. [CrossRef] [PubMed]
47. Ren, X.; Wu, T.; Sun, Y.; Li, Y.; Xian, G.; Liu, X.; Shen, C.; Gracia, J.; Gao, H.-J.; Yang, H.; et al. Spin-polarized oxygen evolution reaction under magnetic field. *Nat. Commun.* **2021**, *12*, 2608. [CrossRef] [PubMed]
48. Tao, F.; Wang, J.; Xu, J.; Chen, G.; Xiao, X.; Li, M.; Zhang, H.; Zhou, X.; Liu, Y.; Wostoupal, O.S.; et al. Spin Polarization Enhanced Ethanol Selectivity in Electrocatalytic $CO_2$ Reduction on the Paramagnetic CuO Surface. *J. Am. Chem. Soc.* **2026**, *148*, 20150–20160. [CrossRef] [PubMed]
49. He, F.; Yan, X.; Pan, X.; Yan, Y.; Gu, J. Spin-Polarized Interfaces Redirect $CO_2$ Reduction from CO to Formate. *Angew. Chem. Int. Ed.* **2026**, e1729522. [CrossRef] [PubMed]
50. Tan, J.; Shelton, J.L.; Wright, D.; Haque, M.A.; Saund, S.S.; Ghoshal, D.; Le, T.H.; Dong, Y.; Smeaton, M.A.; Jungjohann, K.L.; et al. Chirality-induced spin selectivity as a mechanism to control product selectivity during electrochemical $CO_2$ reduction. *Nat. Energy* **2026**, *11*, 1151–1160. [CrossRef]
51. Wang, J.; Ma, X.; Bu, H.; Gao, H.; Liu, Z.; Ding, C.; Zhang, Z.; Dong, M.; Fan, Y.; Zhao, M. Magnetic Regulation of Defect-Engineered $Fe_3GeTe_2$ Monolayer for Enhancing Electrocatalytic $CO_2$ Reduction. *ACS Appl. Energy Mater.* **2025**, *8*, 17003–17013. [CrossRef]
52. Xu, Y.; Xu, B. Thermodynamics of CO Adsorption on Electrodes and Its Implications for Selectivity Control in Electrochemical $CO_2$ Reduction. *ACS Catal.* **2025**, *15*, 7934–7943. [CrossRef]
53. Wang, H.; Sui, H.; Ding, Y.; Yang, Y.; Su, Y.; Li, H. Tailoring $CO_2$ Adsorption Configuration with Spatial Confinement Switches Electroreduction Product from Formate to Acetate. *J. Am. Chem. Soc.* **2025**, *147*, 6095–6107. [CrossRef] [PubMed]

54. Jung, Y.; Abbas, H.G.; Kim, S.; Kim, B.; Cho, J.; Han, S.; Song, H.; Takaoka, Y.; Song, J.T.; Ishihara, T.; et al. Understanding Electrochemical $CO_2$ Reduction Selectivity of Cu Binary Alloys from Electronic Structure Descriptors. *J. Am. Chem. Soc.* **2025**, *147*, 39796–39804. [CrossRef] [PubMed]
55. Peng, B.; She, H.; Wei, Z.; Sun, Z.; Deng, Z.; Sun, Z.; Chen, W. Sulfur-doping tunes p-d orbital coupling over asymmetric Zn-Sn dual-atom for boosting $CO_2$ electroreduction to formate. *Nat. Commun.* **2025**, *16*, 2217. [CrossRef] [PubMed]
56. Wang, M.; Lin, Y.; Xiang, Y.; Sun, Y.; Zhu, Z.-z.; Wu, S.; Cao, X. Curvature Engineering of SiFe Dual-Atom Catalysts for Enhanced $CO_2$ Electroreduction. *J. Phys. Chem. Lett.* **2026**, *17*, 1227–1234. [CrossRef] [PubMed]
57. Jung, H.D.; Deng, J.; Hua, Y.; Jiang, K.; Back, S. Bifurcation of *COOH Pathway Determines HCOOH Formation in $CO_2$ Electroreduction on Bismuth. *Angew. Chem. Int. Ed.* **2026**, *65*, e2216222. [CrossRef] [PubMed]
58. Zhu, Z.; Tang, W.; Wang, J.; Lin, Y.; Li, Z.; Chen, H.; Niu, X.; Chen, J.S.; Wu, R. Regulating the Magnetic Domain of Nickle for Enhanced $CO_2$ Electrochemical Reduction Driven by External Magnetic Field. *Adv. Energy Mater.* **2024**, *15*, 2403624. [CrossRef]
59. Wang, P.; Qu, Y.; Meng, X.; Tu, J.; Zheng, W.; Hu, L.; Chen, Q. A Strong Magnetic Field Alters the Activity and Selectivity of the $CO_2$RR by Restraining C-C Coupling. *Magnetochemistry* **2023**, *9*, 65. [CrossRef]
60. Sun, W.; Gao, Y.; Huang, B.; He, Z.; Yin, S.; Li, F.; Liu, W. Axial O-Bridge Bond Induced Electron High-Spin and Destroyed d-π Conjugation of Fe Single-Atom Sites for Enhanced $CO_2$ Electroreduction. *Adv. Funct. Mater.* **2026**, *36*, e29252. [CrossRef]
61. Ye, K.; Han, Y.; Wu, F.; Hu, M.; Duan, Z.; Hu, P.; Zhang, G.; Ahlquist, M.S.G. Decoding Electric Double Layer Effects on $CO_2$ Electroreduction on Ni-N-C via Multiscale Modeling. *ACS Catal.* **2025**, *16*, 519–527. [CrossRef]
62. Yang, Y.; Fu, G. Resolving sequential electron–proton transfer kinetics for electrochemical $CO_2$ reduction at the Cu(100)/$H_2O$ interface via a quantum-classical framework. *Chem. Sci.* **2026**, *17*, 6419–6425. [CrossRef] [PubMed]
63. Gong, S.; Zhai, Y.; Xia, Q.; Han, X.; Li, W.; Ying, Y.; Wu, J.; Zhou, Y.; She, X.; Wang, Z.; et al. Spin-State Modulation of Atomic Iron Sites Enables Efficient $CO_2$ Electroreduction in Acid Medium. *Angew. Chem. Int. Ed.* **2026**, *65*, e9239759. [CrossRef] [PubMed]
64. Gao, X.; Zhao, Z.; Wu, Z.; Yang, Z.; Guo, K.; Han, J.; Ra, Y.H.; Kong, X.; Zhu, J.; Wang, Y. Multi-Chambered Branches of Hollow Nanoreactors Drive Spatiotemporal Regulation of *CO Intermediate for Efficient $CO_2$-to-$CH_4$ Photoreduction. *Adv. Mater.* **2026**, *38*, e14658. [CrossRef] [PubMed]
65. Shi, Y.; Li, J.; Min, Z.; Wang, X.; Hou, M.; Ma, H.; Zhuang, Z.; Qin, Y.; Sun, Y.; Wang, D.; et al. Adjusting *CO adsorption configuration over tandem trimetallic AuAgCu heterojunction boosts $CO_2$ electroreduction to ethanol via asymmetric C-C coupling. *Sci. China Mater.* **2024**, *68*, 173–179. [CrossRef]
66. Zhu, J.; Chen, J.L.; Qi, X.Z.; Zhao, J.W.; Jiang, X.C.; Li, W.X.; Liu, J.X. Electron-Rich Subnanometer Cu Clusters Facilitate CO-CO Coupling in $CO_2$ Electroreduction. *J. Am. Chem. Soc.* **2026**, *148*, 4008–4019. [CrossRef] [PubMed]
67. Zhang, M.; Zhao, Q.; Gao, Y.; Zheng, L.; Ouyang, J.; Na, N. Manipulating Spin States by Metal Axial Coordination of Active Sites for Generating Valuable $CH_4$ in $CO_2$ Reduction. *Adv. Sci.* **2025**, *13*, e17166. [CrossRef] [PubMed]
68. Yin, B.; Wang, C.; Yang, Y.; Li, Y.; Xu, L.; Gu, J.; Zhang, C. Alternating Magnetic Field Induced Ultra-Active Cu Sites in Trimetal-Organic Frameworks for Low-Overpotential $CO_2$ Electroreduction. *Angew. Chem. Inter. Ed.* **2025**, *64*, e202514255. [CrossRef] [PubMed]
69. Xiong, W.F.; Li, X.H.; Chen, J.L.; Li, Z.; Si, D.H.; Li, H.F.; Cao, R. Polyaniline Encapsulated Cu Nanowires Steering *CO Adsorption Configuration to Enhance Ethanol Selectivity in $CO_2$ Electrocatalysis. *Small* **2026**, *22*, e74080. [CrossRef] [PubMed]
70. Zang, Y.; Liu, Y.; Zhang, L.; Gao, D.; Ou, P.; Lum, Y. Synergistic Catalysis Induced by Zn-Doping for Steering $CO_2$ Electroreduction Pathway Toward Ethanol on Cu Catalyst. *Small* **2026**, *22*, e13647. [CrossRef] [PubMed]
71. Lin, C.-C.; Liu, T.-R.; Lin, S.-R.; Boopathi, K.M.; Chiang, C.-H.; Tzeng, W.-Y.; Chien, W.-H.C.; Hsu, H.-S.; Luo, C.-W.; Tsai, H.-Y.; et al. Spin-Polarized Photocatalytic $CO_2$ Reduction of Mn-Doped Perovskite Nanoplates. *J. Am. Chem. Soc.* **2022**, *144*, 15718–15726. [CrossRef] [PubMed]
72. Qin, X.; Vegge, T.; Hansen, H.A. Modulating Activity and Selectivity of $CO_2$ Electroreductions at Au-Water Interfaces via Engineering Local Cation Condition. *ACS Catal.* **2024**, *14*, 8168–8175. [CrossRef]
73. Re Fiorentin, M.; Risplendi, F.; Salvini, C.; Zeng, J.; Cicero, G.; Jónsson, H. Silver Electrodes Are Highly Selective for CO in $CO_2$ Electroreduction due to Interplay between Voltage Dependent Kinetics and Thermodynamics. *J. Phys. Chem. Lett.* **2024**, *15*, 11538–11545. [CrossRef] [PubMed]
74. Guo, W.; Zhang, Y.; Tian, J.; Liu, Z.; Liu, B.; Li, J. Atomic-scale interface engineering in Bi/$Bi_2O_3$ heterojunctions for selective $CO_2$ photoreduction to methanol. *Nat. Commun.* **2025**, *17*, 983. [CrossRef] [PubMed]
75. Lan, S.; He, H.; Ren, Y.; Fei, P.; Wu, Y.; Zhou, J.; Li, N. Synergistic d-band center modulation and interfacial charge distribution on a $ZrO_2$/CdS catalyst for solar-driven $CO_2$ conversion. *Eng. Energy* **2026**, *20*, 10713. [CrossRef]
76. Ai, L.; Liu, Z.; Zhang, X.; Wang, L.; Jia, D.; Guo, N.; Zha, M.; Tan, C. Engineering cycling of $Cu^{2+}$/$Cu^{+}$ pairs in $Bi_2WO_6$ nanoflowers for boosting photocatalytic $CO_2$ reduction. *J. Colloid Interface Sci.* **2025**, *692*, 137480. [CrossRef] [PubMed]
77. Xiong, R.; Liu, F.; Xiao, X.; Xiao, Y.; Cheng, B.; Lei, S. Dual electronic-spin engineering in cobalt-doped CdS: Photocatalytic pathway switching from competing $H_2$ evolution to selective $CO_2$ reduction. *Chem. Eng. J.* **2025**, *520*, 166224. [CrossRef]

78. Zafar, A.; Shanmugam, S.; Zhang, X. Single Atom Catalysts for Electrochemical $CO_2$ Reduction Reaction: Synthetic Strategies and Mechanistic Insights. *Small* **2025**, *21*, e07483. [CrossRef] [PubMed]
79. Wei, S.; Liu, W.; Xu, L. Unified effects of lanthanoid elements and magnetic fields on the electrocatalytic $CO_2$ reduction reaction. *J. Mater. Chem. A* **2026**, *14*, 23684–23697. [CrossRef]
80. Zhao, Y.; Wang, Y.; Yu, Z.; Song, C.; Wang, J.; Huang, H.; Meng, L.; Liu, M.; Liu, L. Gold Single Atom Doped Defective Nanoporous Copper Octahedrons for Electrocatalytic Reduction of Carbon Dioxide to Ethylene. *ACS Nano* **2025**, *19*, 4505–4514. [CrossRef] [PubMed]
81. Yari, F.; Offenthaler, S.; Vala, S.; Krisch, D.; Schöfberger, W. Efficient electroreduction of $CO_2$ to $C_1$ and $C_2$ products using atomically dispersed boron N-C@graphite catalysts. *Energy Adv.* **2025**, *4*, 1443–1454. [CrossRef] [PubMed]
82. Li, X.; Zhao, B.; Wan, R.; Wang, J.; Li, Z. Single-Atom Transition Metals Anchored NbS2: Electrocatalytic Reduction of $CO_2$ to HCOOH. *J. Phys. Chem. C* **2025**, *129*, 20931–20937. [CrossRef]
83. Choi, J.; Kim, S.; Choi, J.Y.; Park, S.; Je, K.; Liu, S.; Jiang, J.; Yang, S.; Pollock, C.J.; Guzman-Soriano, R.; et al. Dynamic Evolution from Single-Atom Catalysts to Active Nanograins for $CO_2$ Reduction. *J. Am. Chem. Soc.* **2025**, *147*, 37808–37818. [CrossRef] [PubMed]
84. Ding, Y.; Duan, D.; Wu, M.; Zhang, C.; Liu, X.; Liu, Q.; Zhao, Y. Synergistic Effects and Activity Descriptors in Double-Atom Catalysts for Electrochemical $CO_2$ Reduction: A Computational Insight. *Langmuir* **2025**, *41*, 33988–34000. [CrossRef] [PubMed]
85. Su, J.; Ji, Z.; Jiang, D.; Zhao, Y.; Li, F. Coordination-Engineered Double-Atom Catalysts with Inverse Sandwich Structures for $CO_2$ Reduction: A Combined DFT and Machine Learning Study. *J. Phys. Chem. Lett.* **2025**, *16*, 12445–12452. [CrossRef] [PubMed]
86. Koua, K.A.J.; Peng, J.; Zhang, P.; Li, N. Unveiling the magnetic ordering effect in La-doped $Ti_3C_2O_2$ MXenes on electrocatalytic $CO_2$ reduction. *J. Mater. Chem. A* **2024**, *12*, 303–313. [CrossRef]
87. Hu, X.; Li, Q.; Li, W.; Deng, Y.; Liu, D.; Zhang, Y.; Yuan, R.; Ma, Z.; Zhang, J.; Sa, R. Spin-polarized binuclear transition metal doping on g-$C_3N_4$ for photocatalytic $CO_2$ reduction to $C_2$ products: A DFT study. *Mol. Catal.* **2025**, *572*, 114798. [CrossRef]
88. Liao, Y.; Liu, J.; Chen, H.; Yi, Y.; Xi, X.; Liu, J.; Wang, L.; Zhang, J.; Fu, X.-Z.; Luo, J.-L. Unraveling Double-Exchange Effect Coupling Spin Modulation of $Sr_2Fe_{1.5}Mo_{0.5}O_{6-\delta}$ Electrocatalyst for Solid Oxide Cells. *J. Am. Chem. Soc.* **2025**, *147*, 21003–21013. [CrossRef] [PubMed]
89. Gu, Q.; Xin, Y.; Sun, M.; Zhao, Y.; Liao, Y.; Zhang, Y.; Chen, Z.; Cui, Y.; Zhang, L.; Peng, Y.K.; et al. Dual-Spin Centers in a Grid-like Covalent Organic Framework Promote Near-Unity $CO_2$ Electroreduction. *J. Am. Chem. Soc.* **2026**, *148*, 3570–3582. [CrossRef] [PubMed]
90. Liu, Y.; Deng, Q.; Yao, Z.; Liang, T.; Zhang, S.; Zhu, T.; Xing, C.; Pan, J.; Yu, Z.; Liang, K.; et al. Inducing spin polarization via Co doping in the $BiVO_4$ cell to enhance the built-in electric field for promotion of photocatalytic $CO_2$ reduction. *J. Colloid Interf. Sci.* **2024**, *664*, 500–510. [CrossRef] [PubMed]
91. Karbalaei Akbari, M.; Shrestha, K.; Aljammal, N.; Pourvahabi Anbari, A.; Cui, Y.; Zhuiykov, S. Magnetic-Field-Assisted $CO_2$ Electroreduction at Precision-Engineered Ga-Gd Oxide Nanodomain Interfaces. *Precis. Chem.* **2026**, *4*, 850–866. [CrossRef] [PubMed]
92. Yang, Z.; Hu, B.; Wang, X.; Selishchev, D.; Zhang, G. Enhanced Photocatalytic $CO_2$ Reduction over Ni-doped $Bi_4O_5Br_2/NiCo_2O_4$ Heterojunction: Synergistic Enhancement Effect between Spin Polarization and Built-in Electric Field. *ACS Sustain. Chem. Eng.* **2025**, *13*, 1095–1105. [CrossRef]
93. Liu, P.; Ma, H.; Qin, Y.; Li, J.; Li, F.; Ye, J.; Guo, Q.; Su, N.; Gao, C.; Xie, L.; et al. Enhancing C-C Bond Cleavage of Glycerol Electrooxidation Through Spin-Selective Electron Donation in Pd-$PdS_2$-$Co_x$ Heterostructural Nanosheets. *Angew. Chem. Inter. Ed.* **2025**, *64*, e202506032. [CrossRef] [PubMed]
94. Wang, Y.; Wen, R.; Liu, Y.; Huang, Y.; Tan, X.; Yu, Z.; Yao, Z.; Hou, Y. Co doping and oxygen vacancies induced spin polarization and full-space electric field in $ZnSn(OH)_6$ for boosting photocatalytic $CO_2$ reduction via accelerating directional carriers separation. *Appl. Catal. B Environ. Energy* **2026**, *382*, 125916. [CrossRef]
95. Wang, Y.-b.; Wang, X.-h.; Ji, L.-f.; Li, Y.-l.; Liu, S.-j.; Mu, H.-y.; Liu, Y.; Hao, Y.-j.; Li, F.-t. Electron polarization constructing the "frustrated" electron-hole of the Cu-Vo-Ti sites to photocatalytic low concentration $CO_2$. *Appl. Catal. B Environ. Energy* **2025**, *378*, 125605. [CrossRef]
96. Wang, W.; Zhang, M.; Zhou, J.; Fan, B. Regulation of transition metal atoms supported on defective h-BN by adjacent monovacancies for electrochemical $CO_2$ reduction: Mechanism and d-band spin-polarization effect. *J. Mater. Chem. A* **2025**, *13*, 20825–20837. [CrossRef]
97. Zhao, X.; Wei, J.; Li, J.; Li, X.; Guan, A.; Chen, P.; Zhou, L.; Tian, J.; Pan, J.; Luo, B.; et al. Spin-polarized charge transfer in a Z-scheme Mn: $CsPbBr_3$/Zinc phthalocyanine heterojunction for efficient $CO_2$ photoreduction. *J. Alloys Compd.* **2026**, *1050*, 185883. [CrossRef]
98. Feng, Z.; Tang, H.; Hu, C.; Shen, K.; Chen, L.; Li, Y. Multidimensional coordination engineering of single-atom catalysts for boosting electrochemical $CO_2$ reduction. *J. Energy Chem.* **2026**, *114*, 929–935. [CrossRef]

99. Song, J.; Shi, L.; Wei, J.; Deng, M.; Qin, Z.; Yang, L.; Zheng, J.; Jiang, W.; Yao, L.; Dai, Z. Enhancing $CO_2$ electroreduction over iron-nitrogen-doped carbon catalysts by axial bromine coordination. *Carbon Capture Sci. Technol.* **2025**, *17*, 100534. [CrossRef]
100. Wei, G.; Mao, Z.; Liu, L.; Hao, T.; Zhu, L.; Xu, S.; Wang, X.; Tang, S. Rigidly Axial O Coordination-Induced Spin Polarization on Single Ni-$N_4$-C Site by MXene Coupling for Boosting Electrochemical $CO_2$ Reduction to CO. *ACS Appl. Mater. Interface* **2024**, *16*, 52233–52243. [CrossRef] [PubMed]
101. Zhao, Z.; Tan, C.; Sun, P.; Li, F.; Wang, X. Electrochemical $CO_2$-to-CO via enriched oxygen vacancies at gold/ceria interfaces. *J. Mater. Chem. A* **2024**, *12*, 21716–21722. [CrossRef]
102. Hao, Q.; Tang, Q.; Zheng, L.; Liu, K.; Wu, J.; Lu, J. Specific construction of asymmetric carbon-nickel-chlorine single-atom sites via carbon vacancy engineering for efficient $CO_2$ electroreduction. *Nat. Commun.* **2025**, *16*, 8365. [CrossRef] [PubMed]
103. Arkasalerks, P.; Sakulaue, P.; Chakthranont, P.; Kongpatpanich, K.; Nueangnoraj, K. Defect-engineered N-doped carbon stabilizes $Cu^+$ active sites for bifunctional $CO_2$ electroreduction to CO and formate. *RSC Adv.* **2026**, *16*, 4535–4548. [CrossRef] [PubMed]
104. Jin, Z.; Zhang, J.; Qiu, J.; Hu, Y.; Di, T.; Wang, T. Nitrogen vacancy-induced spin polarization of ultrathin zinc porphyrin nanosheets for efficient photocatalytic $CO_2$ reduction. *J. Colloid Interface Sci.* **2023**, *652*, 122–131. [CrossRef] [PubMed]
105. Wei, S.; Liu, W.; Bai, P.; Yang, C.; Kong, X.; Xu, L. Magnetic fields promote electrocatalytic $CO_2$ reduction via subtle modulations of magnetic moments and molecular bonding. *EEH* **2024**, *3*, 247–255. [CrossRef] [PubMed]
106. Karki, N.; Wilson, A.J. Modulation of Selectivity in Electrocatalytic $CO_2$ Reduction with a Magnetic Field and Imidazolium Ionic Liquids. *J. Phys. Chem. C* **2025**, *129*, 14356–14365. [CrossRef]
107. Karki, N.; Marquina, I.G.; Hemmer, J.V.; Yu, Y.; Wilson, A.J. Suppressing Competing Solvent Reduction in $CO_2$ Electroreduction with a Magnetic Field. *J. Phys. Chem. Lett.* **2024**, *15*, 7045–7054. [CrossRef] [PubMed]
108. Li, H.; Liu, C.; Li, D.; Zhu, Y.; Liu, M.; Zhao, S.; Sun, Z. Machine Learning-Assisted Screening and Performance Prediction of Single-Atom Catalysts for Electrocatalytic $CO_2$ Conversion to CO. *Energy Fuels* **2025**, *39*, 17924–17932. [CrossRef]
109. Chen, H.; Yin, J.; Li, J.; Wang, X. Theoretical High-Throughput Screening of Single-Atom $CO_2$ Electroreduction Catalysts to Methanol Using Active Learning. *Engineering* **2025**, *52*, 172–182. [CrossRef]
110. Xixue, H.; Ruoxin, M.; Zekun, Z.; Luping, Z.; Jiqun, L.; Wei, Y.; Hao, X. From data to catalysis: Advances and prospects of machine learning-driven electrocatalytic $CO_2$ reduction. *Green Chem.* **2026**, *28*, 9940–9958. [CrossRef]
111. Zhang, Z.; Jiang, S.; Chen, T.; Zhang, S.; Tan, J.; Zhou, Y.; Yan, Y.; Li, H.; Liu, M. Machine learning and multi-scale descriptor frameworks for accelerated discovery of $CO_2$ electrocatalysts. *Chem. Eng. J.* **2026**, *536*, 175822. [CrossRef]
112. Wang, Y.; Wu, Z.; Jiang, Y.; Zhang, D.; Wang, Q.; Wang, C.; Li, H.; Jia, X.; Fan, J.; Li, H. Bridging Theory and Experiment: Machine Learning Potential-Driven Insights into pH-Dependent $CO_2$ Reduction on Sn-Based Catalysts. *Adv. Funct. Mater.* **2025**, *35*, e06314. [CrossRef]
113. Chen, H.; Qiu, J.; Tew, Y.S.; Wang, X. Autonomous computational catalysis through an agentic research system. *ChemRxiv* **2026**. [CrossRef] [PubMed]
114. Ren, Q.; He, Y.; Sun, Y.; Zhang, S.; Dong, F. Visualizing the dynamic evolution of light-sensitive $Cu^{1+}/Cu^{2+}$ sites during photocatalytic $CO_2$ reduction with an advanced in situ EPR spectroscopy. *Sci. Bull.* **2025**, *70*, 1097–1106. [CrossRef] [PubMed]
115. Li, H.; Hu, Z.; Zuo, F.; Li, Y.; Liu, M.; Liu, H.; Li, Y.; Li, Q.; Ding, Y.; Wang, Y.; et al. Real-time tracking of electron transfer at catalytically active interfaces in lithium-ion batteries. *Proc. Natl. Acad. Sci. USA* **2024**, *121*, e2320030121. [CrossRef] [PubMed]


**Disclaimer/Publisher's Note:** The statements, opinions and data contained in all publications are solely those of the individual author(s) and contributor(s) and not of MDPI and/or the editor(s). MDPI and/or the editor(s) disclaim responsibility for any injury to people or property resulting from any ideas, methods, instructions or products referred to in the content.